Functional observability and subspace reconstruction in nonlinear systems

Arthur N. Montanari,[1,*] Leandro Freitas,[2] Daniele Proverbio,[1,3] and Jorge Gonçalves[1,4]
[1]*Luxembourg Centre for Systems Biomedicine, University of Luxembourg,*
7 avenue des Hauts-Fourneaux, L-4362 Esch-sur-Alzette, Luxembourg
[2]*Department of Industrial Automation and Information Technology, Instituto Federal de Educação,*
Ciência e Tecnologia de Minas Gerais, Campus Betim, Rua Itaguaçu 595, 32677-562 Betim, MG, Brazil
[3]*College of Engineering, Mathematics and Physical Sciences, University of Exeter, Exeter EX4 4QL, United Kingdom*
[4]*Department of Plant Sciences, University of Cambridge, Cambridge CB2 3EA, United Kingdom*

(Received 19 July 2022; accepted 2 December 2022; published 16 December 2022)

Time-series analysis is fundamental for modeling and predicting dynamical behaviors from time-ordered data, with applications in many disciplines such as physics, biology, finance, and engineering. Measured time-series data, however, are often low dimensional or even univariate, thus requiring embedding methods to reconstruct the original system's state space. The observability of a system establishes fundamental conditions under which such reconstruction is possible. However, complete observability is too restrictive in applications where reconstructing the entire state space is not necessary and only a specific subspace is relevant. Here, we establish the theoretic condition to reconstruct a nonlinear functional of state variables from measurement processes, generalizing the concept of functional observability to nonlinear systems. When the functional observability condition holds, we show how to construct a map from the embedding space to the desired functional of state variables, characterizing the quality of such reconstruction. The theoretical results are then illustrated numerically using chaotic systems with contrasting observability properties. By exploring the presence of functionally unobservable regions in embedded attractors, we also apply our theory for the early warning of seizure-like events in simulated and empirical data. The studies demonstrate that the proposed functional observability condition can be assessed *a priori* to guide time-series analysis and experimental design for the dynamical characterization of complex systems.

DOI: 10.1103/PhysRevResearch.4.043195

I. INTRODUCTION

Reconstructing the state space of complex dynamical systems is a key step for their quantitative understanding and forecasting. To do so, time-series analysis methods have been developed to characterize and model dynamical behaviors from recorded time-ordered data. In practice, such methods are constrained by the available measurement processes and data quality. Data are often irregularly sampled, noisy, relatively short, and univariate. In cases that measured time series are expected to be lower dimensional compared to the system dynamics, the original state space can be reconstructed with embedding methods [1–4]. Embedding has been successfully applied across many fields, including for the characterization of chaotic dynamics [5,6], ecological and economic modeling [7,8], financial forecasting [9,10], medical diagnosis [11,12], and detection of dynamical transitions in palaeoclimate data [13] and oil-water flows [14]. These applications assume that an embedding is possible, that is, that a map from the time-series data to the original system's state space exists. However, such assumption may not hold in general: An established link between embedding and observability theories shows that reconstructing the *entire* original system is not always possible or suitable depending on the available time series [15,16].

The *a priori* conditions under which the entire system state can be reconstructed from available measurements are determined by the observability property [17]. In the linear case, observable systems satisfy the necessary and sufficient conditions for the inference of the full-state of the system, for example, via embedding methods and state estimators like Luenberger observers [18] or Kalman filters [19]. For nonlinear systems, a generalized notion of observability [20] sets a sufficient condition for the existence of an invertible mapping (diffeomorphism) between the system's original state space and the differential embedding space constructed from a given measurement function [15,16].

Not only the relation between embedding and observability determines the possibility of reconstructing the original dynamical system from the embedding of time-series data, but it also characterizes *how good* such reconstruction is. For example, the embedding space of the Rössler system was empirically shown to have singularity points depending on the measured variable [21], which was later theoretically proven to be a consequence of unobservable regions in the original

---

[*] arthur.montanari@uni.lu

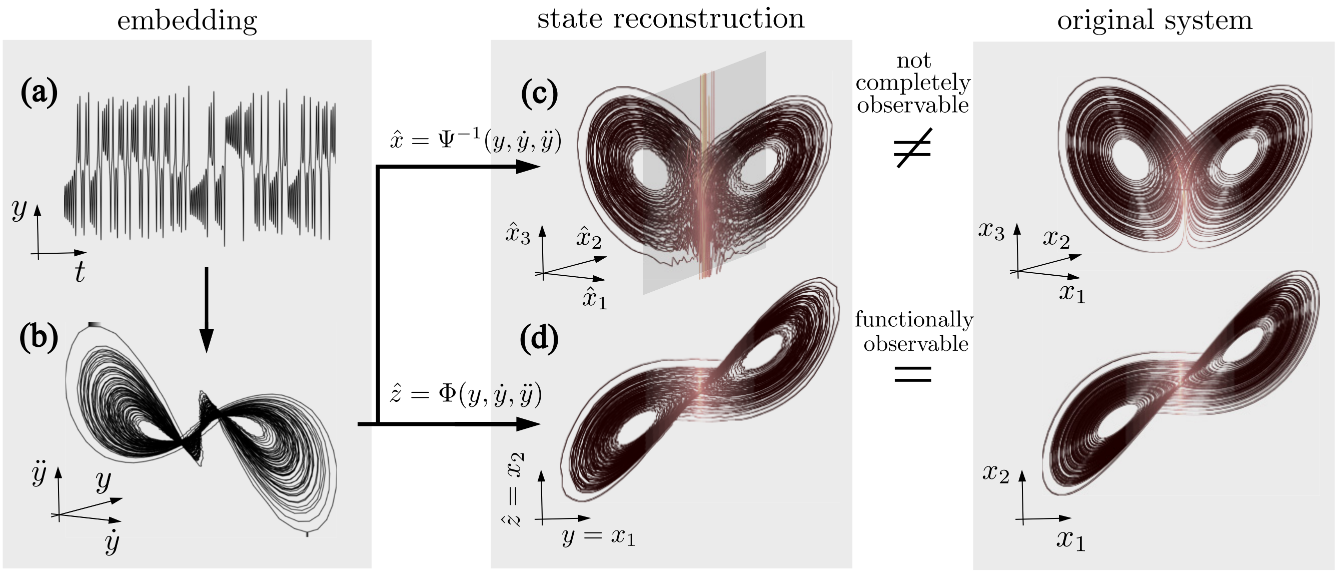

FIG. 1. Functional observability vs complete observability for the reconstruction of the Lorenz attractor from time-series data. (a) Time-series data $y = h(\boldsymbol{x}) = x_1$ measured from one of the system's state variables. (b) Differential embedding coordinates of the time-series data. (c) Reconstruction of the original coordinates of the Lorenz system from the differential embedding. The system is unobservable at the shaded plane ($x_1 = 0$) and, therefore, the reconstructed attractor (left side) shows large errors closer to this region compared to the ground-truth (unmeasured) attractor (right side). (d) Reconstruction of the low-dimensional subspace (x_1, x_2) of the Lorenz attractor. The system is functionally observable everywhere with respect to the functional $z = g(\boldsymbol{x}) = x_2$ and, therefore, the reconstructed subspace (left side) is accurate compared to the ground-truth subspace (right side). Brighter colors correspond to states of the attractor closer to the system's unobservable plane.

space [22]. Another case is the well-known Lorenz system: Figures 1(a)–1(c) shows that unobservable regions hamper the quality of the attractor reconstruction from an embedded time series. Consequently, the applicability and performance of methods based on embedding [23–25] and state estimation [26–28] are highly dependent on the observability properties of the system. Building from chaotic systems, often used as benchmark cases due to their short horizon of predictability, observability studies showed the potential to foster further discoveries in complex systems, including neuronal models [29,30], metabolic reactions [31], ecological systems [32], and networks [33–38].

For many systems and applications, although, complete observability is a condition that may be too restrictive. In practice, even if the original state space is not entirely observable (reconstructible), one may focus on particular subspaces (e.g., state variables) that are relevant to the considered applications. Examples include the estimation of the phase variable of nonlinear oscillators for synchronization analysis of chaotic systems [21,39,40], modeling of climate dynamics [41], and forecasting of financial crashes [42]; the positioning and tracking of a particular spatial coordinate (e.g., altitude) in autonomous aerial vehicles from indirect measurements [43]; or the inference of control variables (which dictate how close a system is to a bifurcation) for the early warning of transitions from healthy to disease states in atrial fibrillation [44] and epileptic seizures [45].

These practical problems motivate the concept of *functional observability* [46,47], which establishes conditions under which a desired functional of the system variables can be inferred from the available measurements (e.g., via the design of functional observers [46,48,49]). However, in spite of several applications designed for feedback control [49,50], fault detection [51], and, more recently, large-scale networks [52], the functional observability property is still restricted to linear dynamical systems. Therefore, a theory to establish conditions for the reconstruction of a *nonlinear* functional of a *nonlinear* system, and that provides guidance on how to perform and leverage this reconstruction, is still missing.

In this paper, we provide a generalization of the functional observability property to nonlinear dynamical systems. This establishes a sufficient condition for the reconstruction of a nonlinear functional of state variables from a (possibly nonlinear) measurement function. If the system is functionally observable, we show how to determine the mapping between the differential embedding space and the original functional sought to be reconstructed, also proposing a coefficient of functional observability to locally characterize the quality of the functional reconstruction. Figure 1 shows that, even though a system may not be completely observable (thus hampering the state-space reconstruction), it might still be functionally observable with respect to some low-dimensional subspace of interest, in which accurate reconstruction is still feasible. To illustrate the theoretical advantages of such framework in interpreting the effects of singularities and symmetries in the embedded state space, we present numerical simulations for chaotic benchmark systems with contrasting observability properties. Finally, we apply our theory for the analysis of a phenomenological model of seizure-like events, known as Epileptor [45]. We demonstrate that the presence of unobservable regions in the Epileptor's attractor can be used to provide early-warning signals of transitions from normal to seizure states in both simulated and empirical data.

The paper is organized as follows. Section II provides a background on the complete observability of dynamical systems. Section III presents the theoretical results for the generalization of functional observability to nonlinear systems. Section IV presents and discusses the numerical results in chaotic benchmark systems. Section V applies the proposed framework for the analysis of the Epileptor model and early warning of seizures. Finally, Sec. VI concludes the paper.

II. BACKGROUND ON OBSERVABILITY OF NONLINEAR SYSTEMS

This section provides background on observability theory for nonlinear systems [20,38,53]. Consider the following nonlinear dynamical system:

$$\begin{aligned}\dot{\boldsymbol{x}} &= \boldsymbol{f}(\boldsymbol{x}),\\ \boldsymbol{y} &= \boldsymbol{h}(\boldsymbol{x}),\end{aligned} \tag{1}$$

where $\boldsymbol{x} \in \mathcal{X} \subseteq \mathbb{R}^n$ is the state vector, $\boldsymbol{y} \in \mathbb{R}^q$ is the output vector (measurements), and $\boldsymbol{f} : \mathcal{X} \mapsto \mathcal{V}(\mathcal{X}) \subseteq \mathbb{R}^n$ and $\boldsymbol{h} : \mathcal{X} \mapsto \mathcal{H}(\mathcal{X}) \subseteq \mathbb{R}^q$ are smooth nonlinear functions. The explicit dependence of time in $\boldsymbol{x}(t)$ and $\boldsymbol{y}(t)$ is often omitted throughout this paper. Let the flow map $\boldsymbol{\Phi}_T(\boldsymbol{x}(t_0)) : \mathcal{X} \mapsto \mathcal{X}$ be the solution of (1),

$$\boldsymbol{\Phi}_T(\boldsymbol{x}(t_0)) := \boldsymbol{x}(t_0 + T) = \boldsymbol{x}(t_0) + \int_{t_0}^{t_0+T} \boldsymbol{f}(\boldsymbol{x}(t))dt. \tag{2}$$

The notion of local observability is formalized as follows.

Definition 1. [20,53] The nonlinear system (1), or the pair $\{\boldsymbol{f}, \boldsymbol{h}\}$, is *locally observable at* $\boldsymbol{x}_0$ if there exists a neighborhood $\mathcal{U} \subseteq \mathcal{X}$ of $\boldsymbol{x}_0$ such that, for every state $\boldsymbol{x}_0 \neq \boldsymbol{x}_1 \in \mathcal{U}$, $\boldsymbol{h} \circ \boldsymbol{\Phi}_T(\boldsymbol{x}_0) \neq \boldsymbol{h} \circ \boldsymbol{\Phi}_T(\boldsymbol{x}_1)$ for some finite time interval $t \in [t_0, t_0 + T]$. Otherwise, $\{\boldsymbol{f}, \boldsymbol{h}\}$ is *locally unobservable at* $\boldsymbol{x}_0$. The system is said to be *locally observable* if it is locally observable at every $\boldsymbol{x}_0 \in \mathcal{X}$.

Definition 1 states that a system is locally observable around an initial state $\boldsymbol{x}(t_0)$ if $\boldsymbol{x}(t_0)$ can be uniquely reconstructed from the measurements $\boldsymbol{y}$ over a finite trajectory, as defined by the composition map $\boldsymbol{h} \circ \boldsymbol{\Phi}_T(\boldsymbol{x}(t_0))$. The local observability of a nonlinear system can be verified through the following algebraic condition.

Definition 2. [53] The observable space $\mathcal{O}(\boldsymbol{x})$ of system (1) is the linear space of functions over the field $\mathbb{R}$ spanned by all functions of the form

$$\mathcal{L}_f^\nu h_j(\boldsymbol{x}), \quad 0 \leqslant \nu \leqslant s, \quad 1 \leqslant j \leqslant q, \tag{3}$$

where $\mathcal{L}_f^\nu h_j(\boldsymbol{x})$ denotes the νth Lie derivative of the jth component of $\boldsymbol{h}(\boldsymbol{x})$ along the vector field $\boldsymbol{f}(\boldsymbol{x})$, and s is the smallest integer such that $\nabla \mathcal{L}_f^k h_j(\boldsymbol{x})$ belongs to the span formed by functions (3) for all $k > s$. By definition, $\mathcal{L}_f^0 h_j(\boldsymbol{x}) := h_j(\boldsymbol{x})$ and

$$\mathcal{L}_f^\nu h_j(\boldsymbol{x}) := \nabla \mathcal{L}_f^{\nu-1} h_j(\boldsymbol{x}) \cdot \boldsymbol{f}(\boldsymbol{x}), \tag{4}$$

where $\boldsymbol{\nabla}$ is the gradient operator with respect to $\boldsymbol{x}$.

Theorem 1. The system (1), or the pair $\{\boldsymbol{f}, \boldsymbol{h}\}$, is locally observable at $\boldsymbol{x}_0$ if there exists a neighborhood $\mathcal{U} \subseteq \mathcal{X}$ of $\boldsymbol{x}_0$ such that

$$\dim\{\nabla \mathcal{O}(\boldsymbol{x})\} = n \tag{5}$$

holds for every $\boldsymbol{x} \in \mathcal{U} \subseteq \mathcal{X}$, where $\mathcal{O}(\boldsymbol{x})$ is the observable space.

Proof. See [20,38,53].

Note that the minimum order ν of Lie derivatives (3) such that condition (5) is satisfied depends on $\{\boldsymbol{f}, \boldsymbol{h}\}$. As a special case, if $\{\boldsymbol{f}, \boldsymbol{h}\}$ are rational functions, it suffices to check condition (5) for the observable space $\mathcal{O}(\boldsymbol{x})$ spanned by functions (3) up to the $(n-1)$th Lie derivative (i.e., $0 \leqslant \nu \leqslant n-1$) [54].

Theorem 1 is a generalization of the observability property of linear systems to nonlinear systems. If the pair $\{\boldsymbol{f}, \boldsymbol{h}\}$ is given by the linear functions $A\boldsymbol{x}$ and $C\boldsymbol{x}$, where $A \in \mathbb{R}^{n\times n}$ and $C \in \mathbb{R}^{q\times n}$, then it follows that the observable space $\mathcal{O}(\boldsymbol{x})$ is defined by the row space of Kalman's observability matrix [17,55]

$$\nabla \mathcal{O}(\boldsymbol{x}) = [C^\mathsf{T} \ \ (CA)^\mathsf{T} \ \ (CA^2)^\mathsf{T} \ \ \dots \ \ (CA^{n-1})^\mathsf{T}]^\mathsf{T} \tag{6}$$

and therefore the linear system is observable if and only if $\text{rank}(\nabla \mathcal{O}) = n$.

A. Observability and embedding

Differential embedding relates the original coordinates of a dynamical system to the derivatives of the measured time series. Formally, given some measurement $\boldsymbol{y} = \boldsymbol{h}(\boldsymbol{x})$ over time $t \in [0, T]$, a differential embedding space $\mathcal{E}$ can be constructed via an appropriate choice of higher-order derivatives of $\boldsymbol{y}$ as coordinates:

$$\mathcal{E} = \text{span}\big\{\nabla y_j^{(\nu)} : j \in \{1, \dots, q\} \text{ and } \nu \in \{0, \dots, s\}\big\}, \tag{7}$$

where $y_j^{(\nu)}$ denotes the νth time derivative of the jth component of the measured signal $\boldsymbol{y}$. If the map $\boldsymbol{\Psi} : \mathcal{X} \mapsto \mathcal{E}$ is a diffeomorphism, then the original state space $\mathcal{X}$ and the embedding space $\mathcal{E}$ are related by a smooth and invertible change of coordinates. Therefore, in applications where the original state space is not available (due to unmeasured state variables), the underlying dynamical system can be assessed via an embedding of the measured time series. In practice, measured time-series data are available in discrete time and hence the embedding can be constructed by either computing their differential coordinates $y_j^{(\nu)}$ (e.g., via regularization methods to denoise the derivatives [56,57]) or using time-delay coordinates $y_j(t - k\tau)$, for some time delay τ and $k \in \mathbb{N}$, following Takens' theorem [58,59].

From Definition 1, $\{\boldsymbol{f}, \boldsymbol{h}\}$ is observable if the map

$$\boldsymbol{\Psi}(\boldsymbol{x}) = \begin{bmatrix} \boldsymbol{y} \\ \dot{\boldsymbol{y}} \\ \vdots \\ \boldsymbol{y}^{(\nu)} \end{bmatrix} = \begin{bmatrix} \boldsymbol{h}(\boldsymbol{x}) \\ \frac{\mathrm{d}\boldsymbol{h}(\boldsymbol{x})}{\mathrm{d}t} \\ \vdots \\ \frac{\mathrm{d}^\nu \boldsymbol{h}(\boldsymbol{x})}{\mathrm{d}t^\nu} \end{bmatrix} = \begin{bmatrix} \mathcal{L}_f^0 \boldsymbol{h}(\boldsymbol{x}) \\ \mathcal{L}_f^1 \boldsymbol{h}(\boldsymbol{x}) \\ \vdots \\ \mathcal{L}_f^\nu \boldsymbol{h}(\boldsymbol{x}) \end{bmatrix} \tag{8}$$

is locally left invertible (injective) for some $0 \leqslant \nu \leqslant s$, where $\mathcal{L}_f^\nu \boldsymbol{h}(\boldsymbol{x}) := [\mathcal{L}_f^\nu h_1(\boldsymbol{x}) \ \dots \ \mathcal{L}_f^\nu h_q(\boldsymbol{x})]^\mathsf{T}$. That is, if $\boldsymbol{x}$ is uniquely determinable from $\boldsymbol{y}$ and its successive derivatives. The map (8) is equivalent to the set of functions (3) spanning the observable space $\mathcal{O}(\boldsymbol{x})$ [15], hence $\boldsymbol{\Psi} : \mathcal{X} \mapsto \mathcal{E} \equiv \mathcal{O}(\boldsymbol{x})$. This equivalence establishes a direct relation between the theories of observability and embedding [15,16]: Following the inverse function theorem [53], Sec. 7.1], $\boldsymbol{\Psi}(\boldsymbol{x})$ is locally invertible if its Jacobian matrix has full (column) rank [i.e., if condition (5) holds]. Therefore, a state $\boldsymbol{x}_0$ is only reconstructible from the differential embedding of its measurements $\boldsymbol{y}$ over a finite time interval if $\boldsymbol{\Psi}$ is locally invertible or, in other words, the system is locally observable at $\boldsymbol{x}_0$.

Note that the choice of differential coordinates $y_j^{(\nu)}$ for the embedding space $\mathcal{E}$ is not unique and that an inappropriate selection of linearly dependent derivatives of $\boldsymbol{y}$ [i.e., functions of form (3)] may lead to $\dim(\nabla\mathcal{E}) < \dim\,(\nabla\mathcal{O}(\boldsymbol{x}))$ [16]. Accordingly, we assume throughout this paper that the embedding space (7) is defined by a minimum selection of linearly independent functions (3) such that $\dim(\nabla\mathcal{E}) = \dim\,(\nabla\mathcal{O}(\boldsymbol{x}))$ around some neighborhood of $\boldsymbol{x}_0$. For example, we consider the embedding space $\mathcal{E} = \{y, \dot{y}, \ddot{y}\}$ for the reconstruction of the Lorenz attractor [Figs. 1(a)–1(c)].

III. FUNCTIONAL OBSERVABILITY OF NONLINEAR SYSTEMS

Complete observability characterizes the sufficient condition for the (local) reconstruction of the *full-state* vector $\boldsymbol{x}$ of a dynamical system (1) from measurements $\boldsymbol{y}$ over finite time. Nonetheless, reconstructing the entire state vector $\boldsymbol{x}$ is often unfeasible or unnecessary in practice, and only a lower-dimensional function or subspace might be of interest, defined as

$$z = \boldsymbol{g}(\boldsymbol{x}), \tag{9}$$

where $z \in \mathbb{R}^r$ is the vector sought to be reconstructed, often with dimension $r \ll n$, and $\boldsymbol{g} : \mathcal{X} \mapsto \mathcal{G}(\mathcal{X}) \subseteq \mathbb{R}^r$ is a nonlinear smooth functional.

In what follows, we provide a generalization of the observability property [20], termed *functional observability*. Given a nonlinear dynamical system (1), functional observability establishes the conditions under which the functional (9) is reconstructible from the measured signal $\boldsymbol{y}$, without necessarily requiring the full state $\boldsymbol{x}$ to be reconstructible. Therefore, a system may be functionally observable with respect to some functional (9) even though it is (completely) unobservable. Our results also generalize the functional observability property, originally established for linear systems [47], to dynamical systems described by a nonlinear vector field $\boldsymbol{f}$, a nonlinear measurement function $\boldsymbol{h}$ and a nonlinear functional $\boldsymbol{g}$. Figure 2 summarizes the relation between our theory and previous papers.

Before presenting the main result, we first formally define functional observability as a generalization of complete observability (Definition 1):

Definition 3. The nonlinear system (1) and (9), or the triple $\{\boldsymbol{f}, \boldsymbol{h}, \boldsymbol{g}\}$, is *locally functionally observable at* $\boldsymbol{x}_0$ if there exists a neighborhood $\mathcal{U} \subseteq \mathcal{X}$ of $\boldsymbol{x}_0$ such that, for every state $\boldsymbol{g}(\boldsymbol{x}_0) \neq \boldsymbol{g}(\boldsymbol{x}_1)$, $\boldsymbol{h} \circ \boldsymbol{\Phi}_T(\boldsymbol{x}_0) \neq \boldsymbol{h} \circ \boldsymbol{\Phi}_T(\boldsymbol{x}_1)$ for some finite time interval $t \in [t_0, t_0 + T]$. Otherwise, $\{\boldsymbol{f}, \boldsymbol{h}, \boldsymbol{g}\}$ is *locally functionally unobservable at* $\boldsymbol{x}_0$. The system is said to be *locally functionally observable* if it is locally functionally observable at every $\boldsymbol{x}_0 \in \mathcal{X}$.

Analogous to Definition 1, Definition 3 states that a system is locally functionally observable around an initial state $\boldsymbol{x}(t_0)$ if the functional $\boldsymbol{g}(\boldsymbol{x}(t_0))$ can be uniquely reconstructed from the measurements $\boldsymbol{y}$ over a finite trajectory. Analogous to Definition 2, we define the functional space related to (9) as follows:

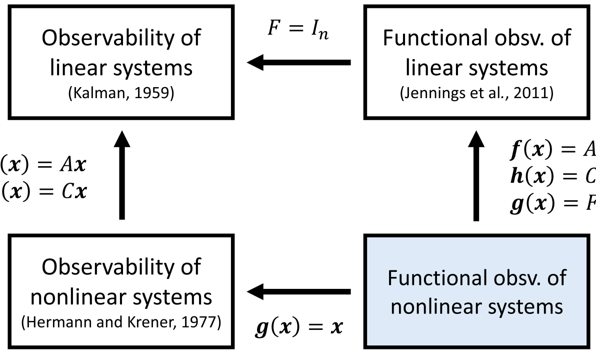

FIG. 2. Functional observability of nonlinear systems and its special cases.

Definition 4. The functional space $\mathcal{F}(\boldsymbol{x})$ of system (1) and (9) is the linear space of functions over the field $\mathbb{R}$ spanned by all functions of the form

$$\mathcal{L}_f^\nu g_j(\boldsymbol{x}), \quad 0 \leqslant \nu \leqslant \mu, \quad 1 \leqslant j \leqslant r, \tag{10}$$

where μ is the smallest integer such that $\nabla\mathcal{L}_f^k g_j(\boldsymbol{x})$ belongs to the span formed by (4) for all $k > \mu$.

Based on Definitions 2 and 4, we now establish the condition for the functional observability analysis of nonlinear systems. Consider a locally unobservable system at $\boldsymbol{x}_0$, i.e.,

$$\dim\{\nabla\mathcal{O}(\boldsymbol{x}_0)\} = k \leqslant n, \quad \forall \boldsymbol{x}_0 \in \mathcal{U} \subseteq \mathcal{X}. \tag{11}$$

Recall the theorem for the decomposition of unobservable systems (Theorem 97 in [53]): There exists a diffeomorphism $\boldsymbol{T}$ on $\mathcal{U}$ such that choosing an appropriate state transformation $\tilde{\boldsymbol{x}} = \boldsymbol{T}(\boldsymbol{x})$ yields the partitioned vector

$$\tilde{\boldsymbol{x}} = \begin{bmatrix} \tilde{\boldsymbol{x}}_a \\ \tilde{\boldsymbol{x}}_b \end{bmatrix}, \tag{12}$$

where $\tilde{\boldsymbol{x}}_a \in \mathbb{R}^k$ and $\tilde{\boldsymbol{x}}_b \in \mathbb{R}^{n-k}$ correspond, respectively, to the observable and unobservable parts of the system in some neighborhood of $\boldsymbol{T}(\boldsymbol{x}_0)$. The transformed vector field is now given by

$$\tilde{\boldsymbol{f}}(\tilde{\boldsymbol{x}}) \equiv \tilde{\boldsymbol{f}}(\tilde{\boldsymbol{x}}_a, \tilde{\boldsymbol{x}}_b) = \begin{bmatrix} \tilde{\boldsymbol{f}}_a(\tilde{\boldsymbol{x}}_a) \\ \tilde{\boldsymbol{f}}_b(\tilde{\boldsymbol{x}}_a, \tilde{\boldsymbol{x}}_b) \end{bmatrix}, \tag{13}$$

where $\tilde{\boldsymbol{f}}_a : \mathbb{R}^k \mapsto \mathbb{R}^k$ and $\tilde{\boldsymbol{f}}_b : \mathbb{R}^n \mapsto \mathbb{R}^{n-k}$, and the transformed measurement function is given by

$$\tilde{\boldsymbol{h}}(\tilde{\boldsymbol{x}}) \equiv \tilde{\boldsymbol{h}}(\tilde{\boldsymbol{x}}_a) = \boldsymbol{h}(\boldsymbol{T}^{-1}(\tilde{\boldsymbol{x}})), \tag{14}$$

which will only depend on $\tilde{\boldsymbol{x}}_a$.

After this change of coordinates, the system (1) and (9) is given by

$$\begin{aligned} \begin{bmatrix} \dot{\tilde{\boldsymbol{x}}}_a \\ \dot{\tilde{\boldsymbol{x}}}_b \end{bmatrix} &= \begin{bmatrix} \tilde{\boldsymbol{f}}_a(\tilde{\boldsymbol{x}}_a) \\ \tilde{\boldsymbol{f}}_b(\tilde{\boldsymbol{x}}_a, \tilde{\boldsymbol{x}}_b) \end{bmatrix}, \\ \boldsymbol{y} &= \tilde{\boldsymbol{h}}(\tilde{\boldsymbol{x}}_a), \\ z &= \tilde{\boldsymbol{g}}(\tilde{\boldsymbol{x}}_a, \tilde{\boldsymbol{x}}_b). \end{aligned} \tag{15}$$

We now note that if the following condition

$$\dim\{\nabla\mathcal{O}(\boldsymbol{x}_0)\} = \dim\{\nabla\mathcal{O}(\boldsymbol{x}_0),\, \nabla\mathcal{F}(\boldsymbol{x}_0)\} \tag{16}$$

holds locally for every $\boldsymbol{x}_0 \in \mathcal{U} \subseteq \mathcal{X}$, then, for some $\tilde{\boldsymbol{x}} = \boldsymbol{T}(\boldsymbol{x})$, we have that $\tilde{\boldsymbol{g}}(\tilde{\boldsymbol{x}}) \equiv \tilde{\boldsymbol{g}}(\tilde{\boldsymbol{x}}_a, \tilde{\boldsymbol{x}}_b) \equiv \tilde{\boldsymbol{g}}(\tilde{\boldsymbol{x}}_a)$ for all $\boldsymbol{x} \in \mathcal{U}$. Consequently, the system is functionally observable given that

$$\tilde{\boldsymbol{g}}(\tilde{\boldsymbol{x}}) \equiv \tilde{\boldsymbol{g}}(\tilde{\boldsymbol{x}}_a) = \boldsymbol{g}(\boldsymbol{T}^{-1}(\tilde{\boldsymbol{x}})) \tag{17}$$

depends only on $\tilde{\boldsymbol{x}}_a$, which is the state vector corresponding to the observable subsystem.

Condition (16) provides a sufficient condition for the local functional observability of the nonlinear system (1) and (9), or the triple $\{\boldsymbol{f}, \boldsymbol{h}, \boldsymbol{g}\}$, at $\boldsymbol{x}_0 \in \mathcal{U}$. Note that this condition is locally equivalent to $\mathcal{F}(\boldsymbol{x}_0) \subseteq \mathcal{O}(\boldsymbol{x}_0)$, that is, that the functional space (the subspace to be reconstructed) should be contained inside the observable space (the subspace reconstructible from the measurement function). The following theorem provides a condition for the functional observability of a nonlinear system that is equivalent to condition (16), but easier to implement since it does not require calculation of the functional space $\mathcal{F}(\boldsymbol{x}_0)$ and the involved higher-order Lie derivatives of $\boldsymbol{g}$.

Theorem 2. The nonlinear system (1) and (9), or the triple $\{\boldsymbol{f}, \boldsymbol{h}, \boldsymbol{g}\}$, is locally functionally observable at $\boldsymbol{x}_0$ if there exists a neighborhood $\mathcal{U} \subseteq \mathcal{X}$ of $\boldsymbol{x}_0$ such that

$$\dim\{\nabla\mathcal{O}(\boldsymbol{x}_0)\} = \dim\{\nabla\mathcal{O}(\boldsymbol{x}_0),\, \nabla\boldsymbol{g}(\boldsymbol{x}_0)\} \tag{18}$$

holds for every $\boldsymbol{x}_0 \in \mathcal{U} \subseteq \mathcal{X}$, where $\mathcal{O}(\boldsymbol{x})$ is the observable space.

Proof. See Appendix A.

The functional observability condition (18) establishes an easy-to-implement test that can be directly verified on the system's equations, that is, functions $\{\boldsymbol{f}, \boldsymbol{h}, \boldsymbol{g}\}$. We note that, even though its derivation is based on the system decomposition (15) presented in (Theorem 97 in [53]), this condition does not require any system transformation or prior knowledge of its equivalence transformation map $\boldsymbol{T}(\boldsymbol{x})$. This provides a significant advantage to analyze the limitations in subspace reconstruction of dynamical systems where deriving the transformation map $\boldsymbol{T}(\boldsymbol{x})$ and its inverse can be computationally intensive, such as the Epileptor model studied in Sec. V.

If the triple $\{\boldsymbol{f}, \boldsymbol{h}, \boldsymbol{g}\}$ is given by linear functions $A\boldsymbol{x}$, $C\boldsymbol{x}$, and $F\boldsymbol{x}$, where $A \in \mathbb{R}^{n\times n}$, $C \in \mathbb{R}^{q\times n}$, and $F \in \mathbb{R}^{r\times n}$, then the observable space $\mathcal{O}(\boldsymbol{x})$ is defined by the row space of the observability matrix (6) and the functional observability of a linear system can be verified using the following rank condition derived in [47,60]:

$$\operatorname{rank}(\nabla\mathcal{O}) = \operatorname{rank}\left(\begin{bmatrix} \nabla\mathcal{O} \\ F \end{bmatrix}\right). \tag{19}$$

If the full-state vector is sought to be reconstructed [i.e., $\boldsymbol{g}(\boldsymbol{x}) = \boldsymbol{x}$], then $\dim\{\nabla\boldsymbol{g}(\boldsymbol{x})\} = n$ and, therefore, the functional observability condition (18) reduces to the complete observability condition (5). Likewise, in the linear case, complete observability is a special case of functional observability by considering $F = I_n$, where I_n is the identity matrix of size n, which reduces condition (19) to the classical condition $\operatorname{rank}(\nabla\mathcal{O}) = n$.

As an illustrative example, consider a dynamical system (1) and (9), or equivalently the triple $\{\boldsymbol{f}, h, g\}$, defined by

$$\boldsymbol{f}(\boldsymbol{x}) = \begin{bmatrix} 2x_1 \\ x_2 + \frac{x_3}{\sqrt{x_1}} \\ 2x_3 \end{bmatrix}, \quad h(\boldsymbol{x}) = x_2, \quad g(\boldsymbol{x}) = x_2 + \frac{x_3}{\sqrt{x_1}}, \tag{20}$$

where $\boldsymbol{x} = [x_1\ x_2\ x_3]^\top \in \mathcal{X}$ and $\mathcal{X} = \{\boldsymbol{x} \in \mathbb{R}^3 \mid x_1 \neq 0\}$ is the region of analysis. Following Theorem 2, we first need to determine a basis for the observable and functional spaces according to Definitions 2 and 4,

$$\nabla\mathcal{O}(\boldsymbol{x}) = \frac{\partial}{\partial\boldsymbol{x}} \begin{bmatrix} h(\boldsymbol{x}) \\ \mathcal{L}_f h(\boldsymbol{x}) \\ \mathcal{L}_f^2 h(\boldsymbol{x}) \\ \mathcal{L}_f^3 h(\boldsymbol{x}) \\ \mathcal{L}_f^4 h(\boldsymbol{x}) \\ \vdots \end{bmatrix} = \begin{bmatrix} 0 & 1 & 0 \\ -\frac{1}{2}\frac{x_3}{x_1^{3/2}} & 1 & \frac{1}{\sqrt{x_1}} \\ -\frac{x_3}{x_1^{3/2}} & 1 & \frac{2}{\sqrt{x_1}} \\ -\frac{3}{2}\frac{x_3}{x_1^{3/2}} & 1 & \frac{3}{\sqrt{x_1}} \\ -2\frac{x_3}{x_1^{3/2}} & 1 & \frac{4}{\sqrt{x_1}} \\ \vdots & \vdots & \vdots \end{bmatrix}, \tag{21}$$

$$\nabla g(\boldsymbol{x}) = \begin{bmatrix} -\frac{1}{2}\frac{x_3}{{x_1}^{3/2}} & 1 & \frac{1}{\sqrt{x_1}} \end{bmatrix}. \tag{22}$$

Rows $\{3, 4, 5, ...\}$ of $\nabla\mathcal{O}(\boldsymbol{x})$ are linear combinations of the first and second rows, leading to $\dim\{\nabla\mathcal{O}\} = 2,\ \forall\boldsymbol{x} \in \mathcal{X}$. This shows that, according to Theorem 1, the pair $\{\boldsymbol{f}, h\}$ is not (completely) observable, i.e., it is not possible to reconstruct the entire state vector $\boldsymbol{x}$ from $y = x_2$. However, the triple $\{\boldsymbol{f}, h, g\}$ may still be functionally observable. By inspection, it is easy to see that $\nabla g(\boldsymbol{x})$ is a linear combination of the rows of $\nabla\mathcal{O}(\boldsymbol{x})$, therefore satisfying condition (18) of Theorem 2 for all $\boldsymbol{x} \in \mathcal{X}$. This example illustrates that, even though a system is locally unobservable, it can still be locally functionally observable.

A. Functional observability and embedding

Complete observability establishes a sufficient condition for the existence of the (local) left-inverse map $\boldsymbol{\Psi}^{-1} : \mathcal{E} \mapsto \mathcal{X}$ from an embedding space to the original state space. Here, we generalize this relation by showing that functional observability establishes a sufficient condition for the existence of a map $\boldsymbol{\Phi} : \mathcal{E} \mapsto \mathcal{G}(\mathcal{X})$ from the embedding space to the subspace sought to be reconstructed. Furthermore, we demonstrate how to construct such a map if the system is functionally observable.

Let $\{\boldsymbol{f}, \boldsymbol{h}, \boldsymbol{g}\}$ be a functionally observable system with an observable space $\mathcal{O}(\boldsymbol{x})$ of local dimension (11). Following (Theorem 97 in [53]), there exists a diffeomorphism $\boldsymbol{T}$ on $\mathcal{U}$ such that the transformation $\tilde{\boldsymbol{x}} = \boldsymbol{T}(\boldsymbol{x})$ partitions the state vector as in (12). Consequently, the triple $\{\boldsymbol{f}, \boldsymbol{h}, \boldsymbol{g}\}$ can now be represented by $\{\tilde{\boldsymbol{f}}, \tilde{\boldsymbol{h}}, \tilde{\boldsymbol{g}}\}$ as in (15). The diffeomorphism $\boldsymbol{T}$ is not unique and can be designed by partitioning it as

$$\boldsymbol{T}(\boldsymbol{x}) = \begin{bmatrix} \tilde{\boldsymbol{x}}_a \\ \tilde{\boldsymbol{x}}_b \end{bmatrix} = \begin{bmatrix} \boldsymbol{\Psi}_a(\boldsymbol{x}) \\ \boldsymbol{\Psi}_b(\boldsymbol{x}) \end{bmatrix}, \tag{23}$$

for some neighborhood $\mathcal{U} \subseteq \mathcal{X}$ of $\boldsymbol{x}_0$. The functions $\boldsymbol{\Psi}_a(\boldsymbol{x})$ and $\boldsymbol{\Psi}_b(\boldsymbol{x})$ can be designed as follows:

(1) Construct a map $\boldsymbol{\Psi}_a(\boldsymbol{x})$ by selecting a minimum set of linearly independent functions of form (3) such that $\dim\{\nabla\boldsymbol{\Psi}_a(\boldsymbol{x})\} = \dim\{\nabla\boldsymbol{\Psi}_a(\boldsymbol{x}), \nabla\mathcal{O}(\boldsymbol{x})\} = k, \forall\boldsymbol{x} \in \mathcal{U} \subseteq \mathcal{X}$.

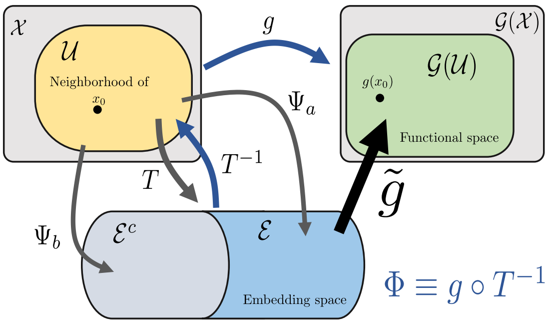

FIG. 3. Commutative diagram of the composition map $\boldsymbol{\Phi}$ (blue path), which maps an embedding space $\mathcal{E}$ to the subspace sought to be reconstructed $\mathcal{G}(\mathcal{U})$.

(2) Construct an arbitrary map $\boldsymbol{\Psi}_b(\boldsymbol{x})$ such that $\dim\{\nabla \boldsymbol{T}(\boldsymbol{x})\} = n$, $\forall \boldsymbol{x} \in \mathcal{U} \subseteq \mathcal{X}$, i.e., $\nabla \boldsymbol{T}(\boldsymbol{x})$ has full rank.

Remind that $\boldsymbol{\Psi}_a(\boldsymbol{x})$ and $\boldsymbol{\Psi}_b(\boldsymbol{x})$ are only valid around a local neighborhood $\mathcal{U} \subseteq \mathcal{X}$ of some state $\boldsymbol{x}_0 \in \mathcal{X}$. The transformation $\boldsymbol{\Psi}_a(\boldsymbol{x}) : \mathcal{U} \mapsto \mathcal{E}$ defines a basis for the embedding space $\mathcal{E}$, which depends only on $\boldsymbol{y}$ and its successive derivatives [see Eq. (7)]. Since $\boldsymbol{y} = \boldsymbol{h}(\boldsymbol{x}) = \tilde{\boldsymbol{h}}(\tilde{\boldsymbol{x}}_a)$ is a function only of $\tilde{\boldsymbol{x}}_a$ [following Eq. (14)], then step 1 guarantees that $\tilde{\boldsymbol{x}}_a \in \mathcal{E}$. Step 2 constructs an arbitrary function $\boldsymbol{\Psi}_b(\boldsymbol{x}) : \mathcal{U} \mapsto \mathcal{E}^c$ that defines a basis to the complement of the embedding space $\mathcal{E}^c$ in order to accomplish the inverse function theorem. Therefore, the designed diffeomorphism $\boldsymbol{T} : \mathcal{U} \mapsto \mathcal{E} \cup \mathcal{E}^c$ has a local inverse map $\boldsymbol{T}^{-1}$.

Since the system is functionally observable, then relation (17) holds and $\boldsymbol{z} = \boldsymbol{g}(\boldsymbol{x}) = \tilde{\boldsymbol{g}}(\tilde{\boldsymbol{x}}_a)$, which depends only on $\tilde{\boldsymbol{x}}_a \in \mathcal{E}$. Therefore, there exists a map $\tilde{\boldsymbol{g}} : \mathcal{E} \mapsto \tilde{\mathcal{G}}(\mathcal{E})$ from the embedding space $\mathcal{E}$ to the functional sought to be reconstructed $\boldsymbol{z} = \tilde{\boldsymbol{g}}(\tilde{\boldsymbol{x}}_a)$. Equivalently, $\boldsymbol{z} = \boldsymbol{g}(\boldsymbol{x})$ can be reconstructed from the composition map $\boldsymbol{\Phi} = \boldsymbol{g} \circ \boldsymbol{T}^{-1}$, which can be locally constructed from the known function $\boldsymbol{g}$ and the designed transformation $\boldsymbol{T}$ according steps 1 and 2. Finally, if the system is functionally observable, then

$$[\boldsymbol{\Phi} : \mathcal{E} \cup \mathcal{E}^c \xmapsto{\boldsymbol{T}^{-1}} \mathcal{U} \overset{\boldsymbol{g}}{\mapsto} \mathcal{G}(\mathcal{U})] \equiv [\tilde{\boldsymbol{g}} : \mathcal{E} \mapsto \tilde{\mathcal{G}}(\mathcal{E})]. \tag{24}$$

Figure 3 illustrates a commutative diagram of the composition map (24). Clearly, if $k = n$, then the relation between complete observability and embedding follows as a special case,

$$\boldsymbol{T}(\boldsymbol{x}) = \boldsymbol{\Psi}_a(\boldsymbol{x}) \text{ and } \boldsymbol{\Phi} : \mathcal{E} \xmapsto{\boldsymbol{\Psi}_a^{-1}} \mathcal{U} \overset{\boldsymbol{g}}{\mapsto} \mathcal{G}(\mathcal{U}). \tag{25}$$

Building on the previous example, given that the system (20) is functionally observable, we demonstrate how to compute (reconstruct) the sought vector $\boldsymbol{z}$ from the measurement signal $\boldsymbol{y}$. To this end, we first decompose the system as in (12) by constructing a diffeomorphism $\boldsymbol{T}(\boldsymbol{x})$ partitioned as (23),

$$\tilde{\boldsymbol{x}} := \left[\begin{array}{c} \tilde{\boldsymbol{x}}_a \\ \hline \tilde{\boldsymbol{x}}_b \end{array}\right] = \boldsymbol{T}(\boldsymbol{x}) = \left[\begin{array}{c} h(\boldsymbol{x}) \\ \mathcal{L}_f h(\boldsymbol{x}) \\ \hline \boldsymbol{\Psi}_b(\boldsymbol{x}) \end{array}\right] \equiv \left[\begin{array}{c} y \\ \dot{y} \\ \hline \boldsymbol{\Psi}_b(\boldsymbol{x}) \end{array}\right], \tag{26}$$

where $\tilde{\boldsymbol{x}}_a \in \mathbb{R}^2$, $\tilde{\boldsymbol{x}}_b \in \mathbb{R}^1$, and $\dim\{\nabla \mathcal{O}\} = k = 2$. Note that $\boldsymbol{\Psi}_a(\boldsymbol{x}) = [y \;\; \dot{y}]^\top$ defines a map between the observable vector and the differential embedding coordinates, while $\boldsymbol{\Psi}_b(\boldsymbol{x})$ is chosen arbitrarily to accomplish the inverse function theorem. Therefore, the diffeomorphism

$$\tilde{\boldsymbol{x}} = \boldsymbol{T}(\boldsymbol{x}) = \left[\begin{array}{c} x_2 \\ x_2 + \frac{x_3}{\sqrt{x_1}} \\ \hline x_1 \end{array}\right] \tag{27}$$

has the inverse function

$$\boldsymbol{x} = \boldsymbol{T}^{-1}(\tilde{\boldsymbol{x}}) = \left[\begin{array}{c} \tilde{x}_3 \\ \tilde{x}_1 \\ \hline (\tilde{x}_2 - \tilde{x}_1)\sqrt{\tilde{x}_3} \end{array}\right], \quad \forall \boldsymbol{x} \in \mathcal{X}. \tag{28}$$

Consequently, z can be computed as

$$\tilde{g}(\tilde{\boldsymbol{x}}) = g(\boldsymbol{T}^{-1}(\tilde{\boldsymbol{x}})) = \tilde{x}_2 = x_2 + \frac{x_3}{\sqrt{x_1}} = \dot{x}_2 = \dot{y}. \tag{29}$$

As expected, we have that $\tilde{g}(\tilde{\boldsymbol{x}}_a, \tilde{\boldsymbol{x}}_b) \equiv \tilde{g}(\tilde{\boldsymbol{x}}_a)$ and, therefore, $g(\boldsymbol{T}^{-1}(\tilde{\boldsymbol{x}}))$ depends only on $\tilde{\boldsymbol{x}}_a$, which is a function of y and its subsequent derivatives.

IV. OBSERVABILITY OF CHAOTIC SYSTEMS

We explore the functional observability property in different types of chaotic dynamical systems with contrasting observability properties, considering different measurement functions as well as functionals sought to be reconstructed. Following the theoretical conditions established in Sec. III, functional (or full-state) reconstruction is possible when the system is functionally (or completely) observable. Beyond this binary characterization of the system observability (i.e., either the system is or is not observable), we show that the accuracy of the reconstructed functional (full-state) vector is dependent on the proximity of the system state to functionally (completely) unobservable regions in the state space. The reconstruction errors are related to the sensitivity of the maps $\boldsymbol{\Psi}^{-1}$ and $\boldsymbol{\Phi}$ to small perturbations [e.g., noise in the measured signals $\boldsymbol{y}(t)$], and can be quantified by the absolute condition number of the inverse maps between the embedding coordinates and the reconstructed state,

$$\kappa(\boldsymbol{\Psi}^{-1}) = \|(\nabla \boldsymbol{\Psi})^{-1}\|, \;\; \kappa(\boldsymbol{\Phi}) = \|\nabla \boldsymbol{g} \cdot (\nabla \boldsymbol{T})^{-1}\|. \tag{30}$$

We address the condition numbers $\kappa(\boldsymbol{\Psi}^{-1})$ and $\kappa(\boldsymbol{\Phi})$ as the coefficients of complete and functional observability, respectively; a nomenclature that was previously adopted for $\kappa(\boldsymbol{\Psi}^{-1})$ in studies restricted to complete observability [16,22,35,38]. Results show that these coefficients can be employed to assess the quality of the (functional) state reconstruction as $\boldsymbol{x}(t)$ approaches unobservable regions: the larger κ, the higher the reconstruction error in the corresponding states.

In what follows, chaotic systems were numerically integrated using a fourth-order Runge-Kutta integrator with time step $dt = 0.01$s for a total simulation time $T = 1100$s, where the initial transient $T_{\text{trans}} = 1000$s was discarded and initial conditions were randomly drawn from a normal distribution [i.e., $x_i(0) \sim \mathcal{N}(0, 1)$, $i = 1, \ldots, n$]. Codes are publicly available at GitHub [61] The symbolic construction of Lie

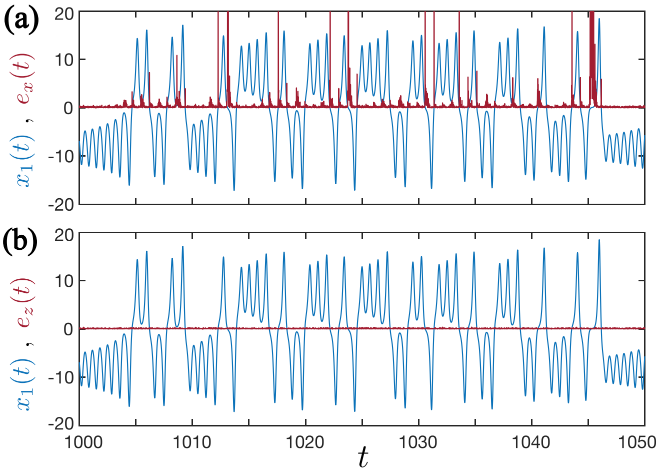

FIG. 4. Reconstruction error (red line) of the Lorenz system as a function of time for the (a) entire state vector $\boldsymbol{x}(t)$ and (b) functional vector $z(t) = x_1(t)$ sought to be reconstructed. Time series of $x_1(t)$ (blue line) is shown for reference.

derivatives (3) spanning the observable space $\mathcal{O}(\boldsymbol{x})$, as well as maps $\boldsymbol{\Psi}$ and $\boldsymbol{\Phi}$, is illustrated in these codes. Note that $\boldsymbol{\Psi}$ is composed by the minimum set of linearly independent functions (3) spanning $\mathcal{O}(\boldsymbol{x})$. Therefore, as a special case for $q = 1$ and $\nu = n - 1$, $\boldsymbol{\Psi}(\boldsymbol{x}) = \mathcal{O}(\boldsymbol{x})$.

A. Lorenz system: Observability and symmetry

The well-known Lorenz'63 system is given by

$$\begin{aligned} \dot{x}_1 &= \sigma(x_2 - x_1), \\ \dot{x}_2 &= Rx_1 - x_2 - x_1x_3, \\ \dot{x}_3 &= x_1x_2 - bx_3, \end{aligned} \quad (31)$$

where $(R, \sigma, b) = (28, 10, 8/3)$ is a set of parameters that leads to a chaotic attractor [Fig. 1(c), right]. Here, we consider that only the state variable x_1 is available for measurement [i.e., $y = h(\boldsymbol{x}) = x_1$] . The observability of the pair $\{\boldsymbol{f}, h\}$ can thus be verified through the observability matrix

$$\nabla\mathcal{O}(\boldsymbol{x}) = \begin{bmatrix} 1 & 0 & 0 \\ -\sigma & \sigma & 0 \\ \sigma^2 + \sigma(\rho - x_3) & -\sigma(\sigma + 1) & -\sigma x_1 \end{bmatrix}. \quad (32)$$

Since $\det(\nabla\mathcal{O}(\boldsymbol{x})) = -\sigma^2 x_1$, then, following condition (5), the system is locally observable at every state $\boldsymbol{x} \in \mathbb{R}^3$ except at $\boldsymbol{x}_0 = [0 \;\; x_2 \;\; x_3]^\top$, where $\dim\{\nabla\mathcal{O}(\boldsymbol{x}_0)\} < 3$.

Given the differential embedding coordinates $\mathcal{E} = \{y, \dot{y}, \ddot{y}\}$ [Fig. 1(b)], the entire state vector $\boldsymbol{x}$ can be reconstructed by computing the inverse map $\mathcal{O}^{-1}(y) : \mathcal{E} \mapsto \mathcal{X}$ [where, as a special case, $\boldsymbol{\Psi}(\boldsymbol{x}) = \mathcal{O}(\boldsymbol{x})$]. Theoretically, existence of this map is not guaranteed only when the system is locally unobservable. In this example, the unobservable subspace corresponds to the exact region in the state space where $x_1 = 0$, which has null Lesbegue dimension. However, in practice, this map degenerates as the system trajectory approaches the neighborhood of $x_1 = 0$, corresponding to a gradual loss of system observability [22]. Figure 4(a) illustrates the reconstruction error $e_x(t) = \|\boldsymbol{x}(t) - \hat{\boldsymbol{x}}(t)\|$, where $\hat{\boldsymbol{x}} = \mathcal{O}^{-1}(y, \dot{y}, \ddot{y})$ is the reconstructed (estimated) state vector, considering a small additive noise to the measured time series: $y(t) = h(\boldsymbol{x}, t) + v(t)$, $v(t) \sim \mathcal{N}(0, 10^{-2})$. Note that noise is largely amplified and the reconstruction error increases significantly as the system state approaches the unobservable region $(x_1(t) \to 0)$.

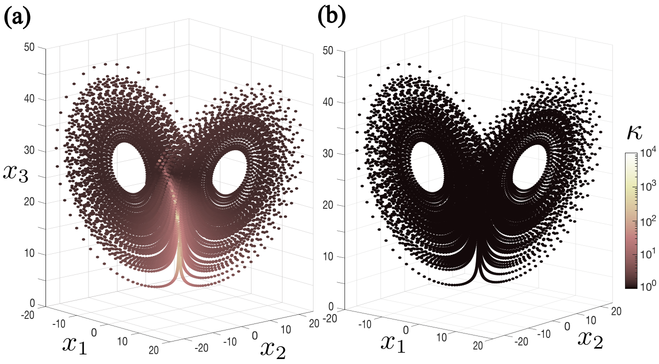

FIG. 5. Coefficient of (a) complete observability and (b) functional observability $[g_1(\boldsymbol{x}) = x_2]$ computed over the state space of the Lorenz attractor.

Despite the unobservability at $x_1 = 0$, the system $\{\boldsymbol{f}, h, g_1\}$ is always functionally observable with respect to the functional $g_1(\boldsymbol{x}) = x_2$, where $\text{row}\,(\nabla g(\boldsymbol{x})) \subseteq \text{row}\,(\nabla\mathcal{O}(\boldsymbol{x}))$, $\forall \boldsymbol{x} \in \mathbb{R}^3$. In practice, $z = g_1(\boldsymbol{x})$ can be reconstructed from the composition map (24) given by

$$\tilde{\boldsymbol{x}} = \left[\begin{array}{c} y \\ \dot{y} \\ \hline x_3 \end{array}\right], \; \boldsymbol{T}^{-1}(\tilde{\boldsymbol{x}}) = \left[\begin{array}{c} \tilde{x}_1 \\ \tilde{x}_1 + \frac{\tilde{x}_2}{\sigma} \\ \hline \tilde{x}_3 \end{array}\right], \; \tilde{g}(\tilde{\boldsymbol{x}}) = y + \frac{\dot{y}}{\sigma}. \quad (33)$$

Figure 4(b) shows the reconstruction error $e_z(t) = \|z(t) - \hat{z}(t)\|$, where $\hat{z} = \Phi(y, \dot{y})$. As expected, since the system is functionally observable for all $\boldsymbol{x} \in \mathbb{R}^3$, the reconstruction error $e_z(t)$ of the functional is not affected by the unobservable region $x_1 = 0$ and remains bounded [see also Fig. 1(d)].

Figure 5 presents the coefficients of observability for the Lorenz system. The coefficient of complete observability increases as $x_1(t) \to 0$, indicating a substantial increase of sensitivity of the local reconstruction map $\boldsymbol{\Psi}^{-1}(\boldsymbol{x})$ to small perturbations, as observed in the large reconstruction errors $e_x(t)$ for $x_1(t) \to 0$ in Fig. 4(a). On the other hand, the coefficient of functional observability remains well-conditioned and constant throughout the entire attractor, which is supported by the insensitivity to noise in the reconstruction error $e_z(t)$ in Fig. 4(b). These results demonstrate that these coefficients can provide proxy indicators of the "practical" consequences of the lack of (functional) observability of these systems as the state approaches (functionally) unobservable regions, where local reconstruction maps become highly sensitivity to noise and, therefore, fail to provide an accurate reconstruction of the original state space.

The Lorenz system is marked by a clear relation between observability and symmetry. Since $h(\boldsymbol{x}) = x_1$ is directly measured and $g(\boldsymbol{x}) = x_2$ is functionally observable, one can observe (reconstruct) the dynamics in the (x_1, x_2) plane of the Lorenz attractor. The functional observability of this plane is directly related to the global invariance of the Lorenz attractor under the map $[x_1 \; x_2 \; x_3]^\top \mapsto [-x_1 \; -x_2 \; x_3]^\top$ [22].

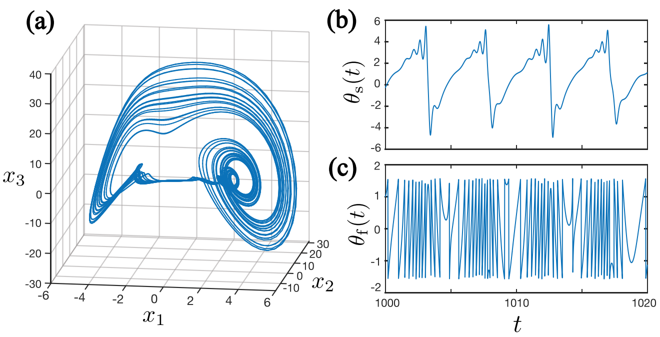

FIG. 6. Cord system. (a) State space of the Cord attractor. (b) Time series of the slow phase $\theta_s(t)$. (c) Time series of the fast phase $\theta_f(t)$.

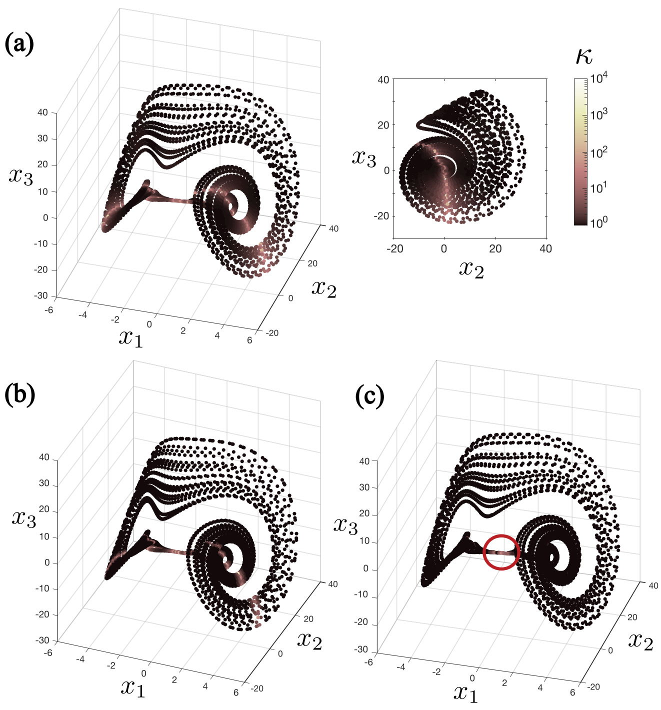

FIG. 7. Coefficient of (a) complete observability, (b) functional observability with respect to $g_1(\boldsymbol{x})$, and (c) functional observability with respect to $g_2(\boldsymbol{x})$ computed over the state space of the Cord attractor.

Given that x_3 is invariant under this symmetry, one can only distinguish which "wing" of the chaotic attractor the system state belongs to at a given time instant t by accurately observing variables x_1 and x_2 [Fig. 1(d)]. Therefore, the functional observability of the triple $\{\boldsymbol{f}, h, g_1\}$ provides the necessary and sufficient information for this characterization based on the measured time series $y(t)$. Moreover, it is evident that the lack of complete observability in the system $\{\boldsymbol{f}, h, g_1\}$ is due to variable x_3, which can be rigorously verified by noting that the functional observability condition (18) is only satisfied for a triple $\{\boldsymbol{f}, h, g_2\}$, $g_2(\boldsymbol{x}) = x_3$, if $x_1 \neq 0$.

B. Cord system: Fast and slow dynamics

The Cord system, a variation of the Lorenz'84 system, is given by [62]

$$\begin{aligned}\dot{x}_1 &= -x_2 - x_3 - ax_1 + aF,\\ \dot{x}_2 &= x_1x_2 - bx_1x_3 - x_2 + G,\\ \dot{x}_3 &= bx_1x_2 + x_1x_3 - x_3,\end{aligned} \tag{34}$$

where $(a, b, F, G) = (0.258, 4.033, 8, 1)$. The chaotic attractor is illustrated in Fig. 6(a). The system dynamics is marked by two oscillation modes with a clear timescale separation [63]. Oscillations in the slow timescale can be approximately monitored by the "slow phase" variable $\theta_s = x_1$ [Fig. 6(b)], in which a full revolution of the system is completed every time the trajectory approaches the cord filament close to the origin (defining the Poincaré section $\mathcal{P} = \{\boldsymbol{x} : x_1 = 0, \dot{x}_1 > 0\}$) [40]. Oscillations in the fast timescale, on the other hand, can be monitored by the "fast phase" variable $\theta_f = \tan^{-1}(x_2/x_3)$ [Fig. 6(c)].

Here, we consider the measured time series $y = h(\boldsymbol{x}) = x_2$ and that the slow and fast phase variables are the functionals sought to be reconstructed, i.e., $g_1(\boldsymbol{x}) = \theta_s$ and $g_2(\boldsymbol{x}) = \theta_f$. Figure 7 shows the coefficients of observability for the Cord system. Full-state reconstruction of the Cord system from the measured time series is not possible for a considerable range of states in the system trajectory [Fig. 6(a)], defined by the plane

$$\begin{aligned}\det(\mathcal{O}(\boldsymbol{x})) = \;& b^2x_3(-aF + 2x_1^2 + x_2 + 2x_3) + 2b^3x_1^2x_2\\ & - b(Gx_1 - aFx_2 + x_2^2 + 3x_1x_3) + x_2^2\\ = \;& 0,\end{aligned} \tag{35}$$

and is expected to be ill conditioned when the system state is close to the vicinity of this plane. The unobservable plane can be visualized in the (x_2, x_3) section of the attractor in Fig. 7(a).

Similarly to the full-state reconstruction problem, the reconstruction of the system's slow timescale [i.e., $g_1(\boldsymbol{x})$] from time-series data of a state variable dominated by a fast timescale (e.g., x_2) is hampered by the lack of observability in a large subspace of the state space, as indicated by the regions with very large coefficients of functional observability in Fig. 7(b). Contrariwise, reconstruction of the fast timescale [i.e., $g_2(\boldsymbol{x})$] from x_2 is well conditioned throughout the entire system trajectory, except as $(x_2, x_3) \to (0, 0)$ [Fig. 7(c), red circle]. The lack of functional observability at this singularity region in the attractor is not surprising: it corresponds exactly to the region in which the fast phase variable θ_f is a (locally) ill-defined function,

$$\nabla\theta_f(\boldsymbol{x}) = \begin{bmatrix} 0 & -\frac{x_3}{\sqrt{x_2^2+x_3^2}} & \frac{x_2}{\sqrt{x_2^2+x_3^2}} \end{bmatrix}, \tag{36}$$

and the fast phase "collapses", undergoing an inversion of its rotational direction [62].

This example illustrates that, even though the system may have a (relatively) large unobservable region $\mathcal{X}_u \subset \mathcal{X}$, one may find that, even in this unobservable region, the system can still be functionally observable with respect to some functional $\boldsymbol{g}(\boldsymbol{x})$ aside from a significantly smaller subregion $\mathcal{X}'_{fu} \subset \mathcal{X}_u$. In this example, the region of interest $\mathcal{X}$ is the Cord attractor $\mathcal{A}$, the "completely" unobservable region $\mathcal{X}_u$ is the 2-dimensional plane defined by (35), and the functionally unobservable region is the 1-dimensional line $\mathcal{X}_{fu} = \{(x_1, 0, 0)\,|\,\boldsymbol{x} \in \mathcal{A}\}$.

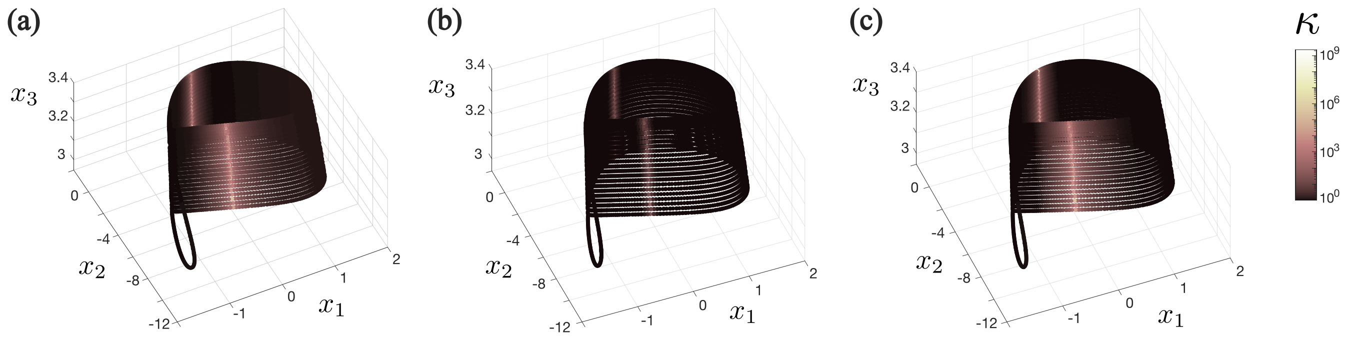

FIG. 8. Coefficients of (a) complete observability, (b) functional observability with respect to $g_1(\boldsymbol{x})$, and (c) functional observability with respect to $g_2(\boldsymbol{x})$ computed over the state space of the HR neuron model, considering the measured time series $y = h_2(\boldsymbol{x})$. Simulations are presented for $(T, T_{\text{trans}}) = (2500, 1500)$.

C. Hindmarsh-Rose system: A neuron model

Building up from the chaotic benchmarks, we now consider a phenomenological model of neuron dynamics given by the Hindmarsh-Rose (HR) model [64],

$$\begin{aligned}\dot{x}_1 &= x_2 - a x_1^3 + b x_1^2 - x_3 + I,\\ \dot{x}_2 &= c - d x_1^2 - x_2,\\ \dot{x}_3 &= r(s x_1 - x_{\text{R}}) - x_3,\end{aligned} \tag{37}$$

where x_1 is the membrane potential, x_2 is the fast recovery current, and x_3 is the slow adaptation current. Providing both a simplification of the biophysical Hodgkin-Huxley neuronal model and a generalization of the FitzHugh-Nagumo model, the HR model can reproduce a wide range of dynamical behaviors, including quiescence and (irregular) spiking and bursting [65]. Moreover, depending on the bifurcation parameters, this system can also shift to chaotic regimes, as investigated both computationally [65] and experimentally [66]. Here, we consider the set of parameters lying in the chaotic regime: $(a, b, c, d, I, r, s, x_{\text{R}}) = (1, 3, 1, 5, 3.25, 0.001, 4, -8/5)$.

The measurement functions $h_1(\boldsymbol{x}) = x_1$, $h_2(\boldsymbol{x}) = x_2$, and $h_3(\boldsymbol{x}) = x_3$ yield observability matrices with determinants given by, respectively, $\det(\mathcal{O}_1(\boldsymbol{x})) = r - 1$, $\det(\mathcal{O}_2(\boldsymbol{x})) = 4d^2x_1^2$, and $\det(\mathcal{O}_3(\boldsymbol{x})) = r^2s^2$. Thus, for the considered set of parameters, $\{\boldsymbol{f}, h_1\}$ and $\{\boldsymbol{f}, h_3\}$ are locally observable everywhere, while $\{\boldsymbol{f}, h_2\}$ becomes locally unobservable only at $x_1 = 0$ [30]. Accordingly, the coefficients of complete observability show a considerable increase as $x_1 \to 0$ [Fig. 8(a)]. One might wonder if, despite the lack of complete observability at $x_1 = 0$, the system $\{\boldsymbol{f}, h_2, g_i\}$ is still functionally observable with respect to, for example, $g_1(\boldsymbol{x}) = x_1$ or $g_2(\boldsymbol{x}) = x_3$. However, unlike the previous examples, the HR model remains locally unobservable at $x_1 = 0$ with respect to both functionals, as observed in the coefficients of functional observability shown in Figs. 8(b) and 8(c). Nevertheless, note that the neighborhood of $x_1 = 0$ where the reconstruction map is (locally) ill conditioned is substantially smaller for $\{\boldsymbol{f}, h_2, g_1\}$ compared compared to $\{\boldsymbol{f}, h_2, g_2\}$. These results suggest that reconstruction of $g_1(\boldsymbol{x})$ is more reliable than $g_2(\boldsymbol{x})$ in the presence of small perturbations as $x_1 \to 0$.

Examining the local maps yield

$$\nabla g_1 \nabla \mathcal{O}_2^{-1} = \left[-\frac{1}{2dx_1} \quad -\frac{1}{2dx_1} \quad 0\right], \tag{38}$$

$$\nabla g_2 \nabla \mathcal{O}_2^{-1} = \left[1-\frac{\xi}{2dx_1^2} \quad \frac{x_1+\xi}{2dx_1^2} \quad \frac{1}{2dx_1}\right], \tag{39}$$

where $\xi = I + x_2 - x_3 - 4ax_1^3 + 3bx_1^2$. The presence of the terms x_1 and x_1^2 in the denominator of Eqs. (38) and (39) elucidate the results shown in Figs. 8(b) and 8(c). The sensitivity to small perturbations in the reconstruction of functional $g_1(\boldsymbol{x})$ is only inversely proportional to the distance between x_1 and the unobservable region, whereas the sensitivity of the reconstruction of $g_2(\boldsymbol{x})$ is inversely proportional to the *quadratic* of this distance—leading to a highly ill-conditioned map for $|x_1| \ll 1$. This theoretical (local) analysis is also supported by computing the reconstruction maps $\boldsymbol{\Phi} : \mathcal{E} \mapsto \mathcal{G}(\mathcal{X})$ and evaluating the corresponding reconstruction performance for each functional. Figure 9 shows that, in the presence of small measurement noise $v(t) \sim \mathcal{N}(0, 0.01)$, reconstruction of $\hat{z}_2 = g_2(\boldsymbol{x})$ yields very poor results, with a high root-mean-square error (RMSE) of 0.4006, compared to the RMSE of 0.0242 for the reconstructed vector $\hat{z}_1 = g_1(\boldsymbol{x})$.

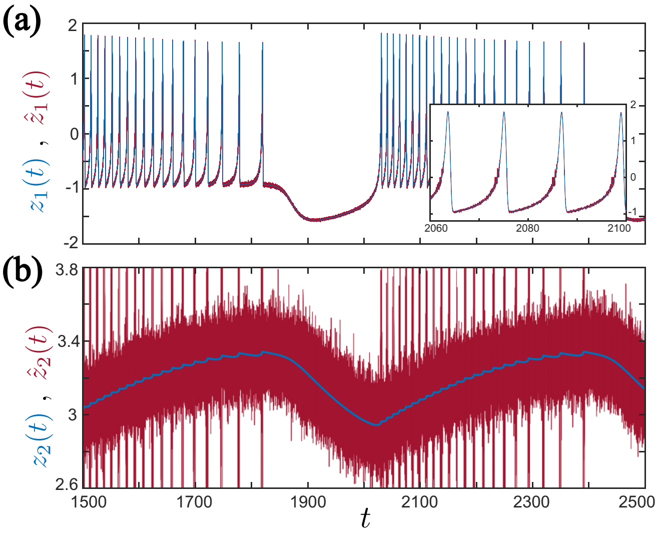

FIG. 9. Reconstructed functional states (a) $\hat{z}_1$ and (b) $\hat{z}_2$ as a function of time (red lines) for the HR neuron model. Time series of $z_1 = g_1(\boldsymbol{x})$ and $z_2 = g_2(\boldsymbol{x})$ (blue lines) are shown for reference. Simulations are presented for $(T, T_{\text{trans}}) = (2500, 1500)$.

As in the Cord example, reconstruction of the slow timescale dynamics [$g_2(\boldsymbol{x}) = x_3$ in the HR model] from time-series data corresponding to a variable dominated by the fast timescale [$h_2(\boldsymbol{x}) = x_2$] is marked by the presence of unobservable regions, which significantly hamper the quality of the reconstruction in the vicinity of these regions. On the other hand, measuring a variable dominated by the fast timescale can still provide accurate reconstruction of other variables dominated by the same timescale [$g_1(\boldsymbol{x}) = x_1$]. This relation between the timescale separation and functional observability of a system, with respect to variables belonging to the same or different timescales than the measured variable, can be observed both in the Cord and HR models.

V. EARLY WARNING OF SEIZURES

Characterizing and predicting epileptic seizures are long-standing challenges in clinical neuroscience [67,68]. Accurate and interpretable methods for the prediction of seizure events will drastically improve epilepsy management, providing early warnings to alert patients or trigger interventions [69]. On top of black-box and data-greedy deep learning algorithms, dynamical-based topological analysis can concur in discovering universal routes to epilepsy and foster new methods for early warning, many of which can be based on the embedding of time-series data [45,70]. We investigate the observability and embedding properties of such application by considering a dynamical model describing seizure dynamics in the brain. The model, termed Epileptor [45], involves bifurcation dynamics to reproduce resting, spiking, and bursting behaviors observed in electroencephalogram (EEG) signals, modeling the multiple timescale oscillations recorded during epileptic seizures. The Epileptor is defined by [45]

$$\begin{aligned}
\dot{x}_1 &= x_2 - f(x_1, x_4) - x_3 + I_1,\\
\dot{x}_2 &= r_2 - 5x_1^2 - x_2,\\
\dot{x}_3 &= \frac{1}{\tau_0}(4(x_1 - r_1) - x_3),\\
\dot{x}_4 &= -x_5 + x_4 - x_4^3 + I_2 + 0.002g(x_1) - 0.3(x_3 - 3.5),\\
\dot{x}_5 &= \frac{1}{\tau_2}(-x_5 + f_2(x_4)), \qquad (40)
\end{aligned}$$

where $(r_1, r_2, I_1, I_2, \gamma) = (-1.6, 1, 3.1, 0.42, 0.01)$ are the system parameters, $(\tau_0, \tau_2) = (2857, 10)$ are the timescale constants, and the coupling functions are given by

$$\begin{aligned}
g(x_1) &= \int_{t_0}^{t} \exp(-\gamma(t-\tau))x_1(\tau)d\tau,\\
f_1(x_1, x_4) &= \begin{cases} x_1^3 - 3x_1^2, & x_1 < 0,\\ (x_4 - 0.6(x_3 - 4)^2)x_1, & x_1 \geqslant 0,\end{cases}\\
f_2(x_4) &= \begin{cases} 0, & x_4 < -0.25,\\ 6(x_4 + 0.25), & x_4 \geqslant -0.25.\end{cases} \qquad (41)
\end{aligned}$$

This model consists of three subsystems with different timescales: (x_1, x_2) governs the system's oscillatory behavior, (x_4, x_5) introduces the spikes and wave components typical in seizure-like events, and x_3 represents a slow permittivity variable that determines how close the system is to the seizure threshold. Due to the slow-fast timescale separation induced by τ_0, x_3 is usually interpreted as a quasi-steady-state parameter [45], enabling bifurcation analysis.

A. Functional observability analysis

Monitoring the permittivity variable x_3 provides an early-warning signal of a dynamical transition from normal to seizure states in the Epileptor model. Despite the phenomenological nature of the model, this permittivity variable is most likely related to slowly changing biophysical parameters (e.g., extracellular processes or ionic concentrations) [45]. Given that such parameters are hardly measurable in biomedical setups, we investigate whether it is possible to infer the permittivity variable [i.e., the functional $z = g(\boldsymbol{x}) = x_3$] from more easily accessible measurements, such as EEG recordings of seizure-like events (modeled as the measurement signal $y = h(\boldsymbol{x}) = x_1 + x_4$ due to its close resemblance to actual EEG data [45]). Figure 10(a) illustrates the dynamics of the functional $z(t)$ and output $y(t)$. Under the assumption that the Epileptor is a proper representation of the underlying process, a functional observability analysis of model (40) can establish if it is feasible to reconstruct this functional and, therefore, provide an early-warning signal of seizure events from EEG data.

Due to the model complexity, an analytical derivation of the functionally unobservable regions of the Epileptor model is hardly tractable. Instead, Figs. 10(b) and 10(c) presents the coefficients of functional observability of the triple $\{\boldsymbol{f}, h, g\}$ computed over the system's attractor. The system alternates between two regions of the attractor, the normal state and the seizure state, as x_3 crosses predetermined thresholds marking bifurcation points (i.e., points in the parameter space where qualitative changes in system dynamics occur). While the coefficients κ are fairly well conditioned in the seizure region of the attractor ($\kappa < 10^2$), the normal region has relatively larger coefficients ($\kappa \approx 10^4$) with two remarkable ill-conditioned singularities ($\kappa > 10^7$) highlighted in Fig. 10(b). This indicates the presence of two functionally unobservable states in the normal region of the Epileptor's state space, one of them located exactly at the saddle-node bifurcation point from normal to seizure regime ($x_3 \approx 2.9$, $\dot{x}_3 < 0$ [71]). Introducing linear additive process noise to the model (40) promotes a larger exploration of system's state space, uncovering other functionally unobservable singularities in the normal region [Fig. 10(c)], including a few in the seizure region. Nonetheless, the analysis remains qualitatively similar between the deterministic and stochastic systems: both show considerably larger values of κ in the normal region compared to the seizure region [see also Fig. 12(b)]. Consequently, high errors are expected in the reconstruction of the permittivity variable from the measured signal $y(t)$ during the normal regime of the Epileptor.

B. Early-warning signals and observability

At first, large coefficients of functional observability in the Epileptor's normal region indicate that reconstructing the slow permittivity variable from EEG data is particularly challenging. However, our analysis established an interesting

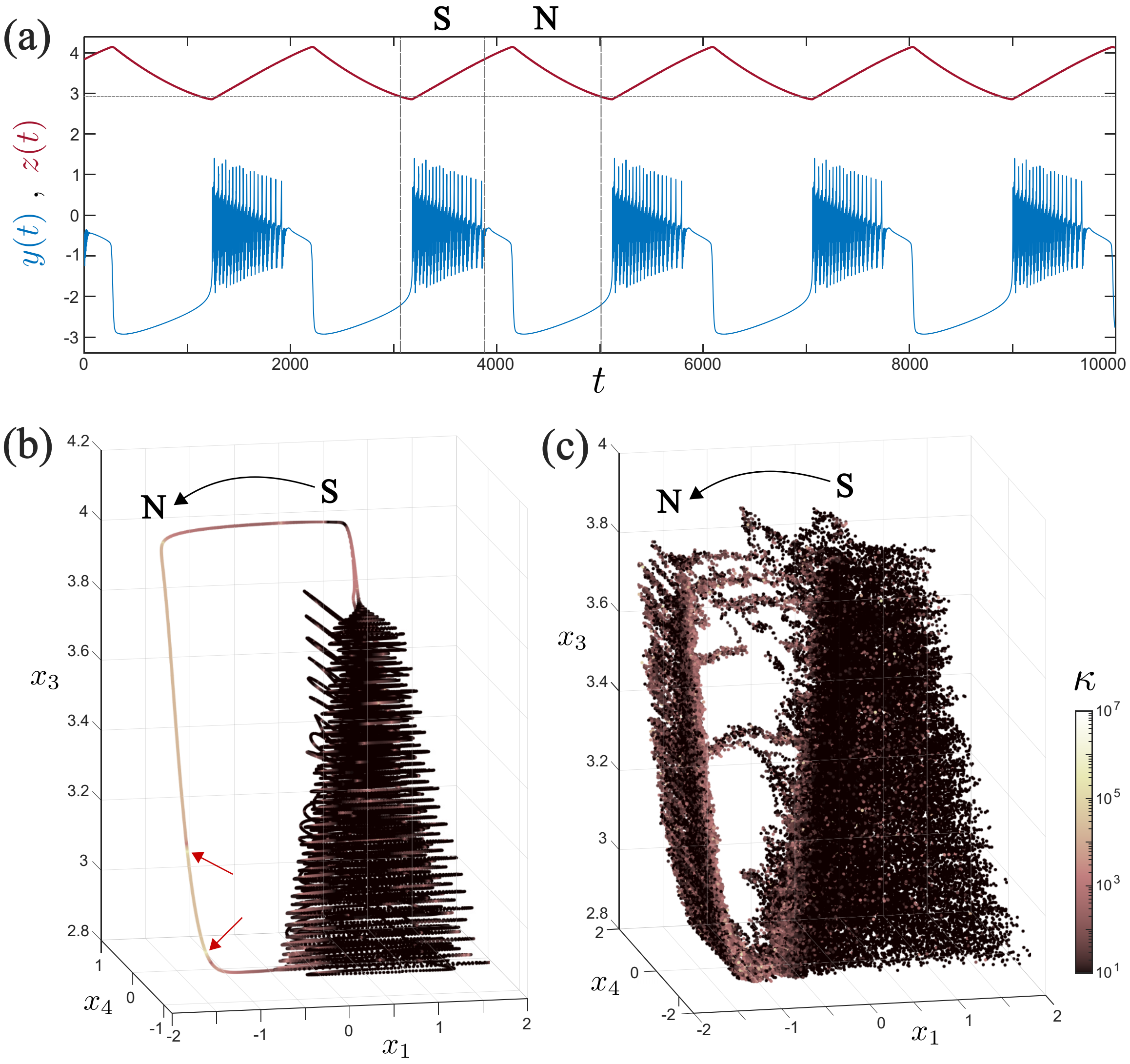

FIG. 10. Functional observability of the Epileptor model. (a) Time series of the measured signal $y(t)$ (modeling EEG data) and the functional $z(t)$ (slow permittivity variable) for the deterministic model. [(b), (c)] Coefficients of functional observability computed over the state space of the Epileptor's attractor, considering (b) deterministic and (c) stochastic representations of the Epileptor. Red arrows point highly functionally unobservable states in the attractor. Transitions from seizure (S) to normal (N) regime in the Epileptor are indicated in the plots. Simulations are presented for $(T, T_{\text{trans}}, dt) = (10^4, 0, 0.01)$ and $\boldsymbol{x}(0) = [0\ -5\ 3\ 0\ 0]^{\mathsf{T}}$. For the stochastic model, the model (40) was numerically integrated using Euler-Maruyama method where additive process noises $\mathcal{N}(0, 0.01)$ and $\mathcal{N}(0, 0.1)$ were introduced to subsystems (x_1, x_2) and (x_4, x_5), respectively.

relation between the Epileptor's observability and topological features: normal (seizure) regions of the attractor correspond to regions with large (small) coefficients of functional observability. This relation can be explored to develop early-warning indicators of seizure-like events in simulated and empirical data.

Typical early-warning signals of critical transitions studied in the literature, such as variance and autocorrelation, are computed from time-series data [72]. Evaluating the system's observability, on the other hand, requires prior knowledge of the system's equations (1), often absent for real-world systems. Theory states that unobservable regions in the state space are associated to the loss of dimension of the observable space [i.e., condition (18) does not hold]. As a consequence, closer to unobservable regions, embedded trajectories squeeze into a small low-dimensional neighborhood due to the loss of diffeomorphism between the embedding space and the original state space [15]. This phenomenon is illustrated in Fig. 11 for the embedded attractors of different dynamical systems with poorly observable regions as well as real-world data. Such local topological feature can be assessed by monitoring the smallest singular value σ_{d_e} computed from an embedded time series with embedding dimension d_e (see Appendix B for details). As $\sigma_{d_e} \to 0$, the effective dimension of the embedded time series drops, implying that the diffeomorphism between the embedded and original attractors is not locally preserved (and, therefore, the system is locally unobservable). In what follows, we apply the coefficient σ_{d_e}, hereby referred to as "time-series-based singular value decomposition" (tSVD), as a proxy measure of the system's observability computed from

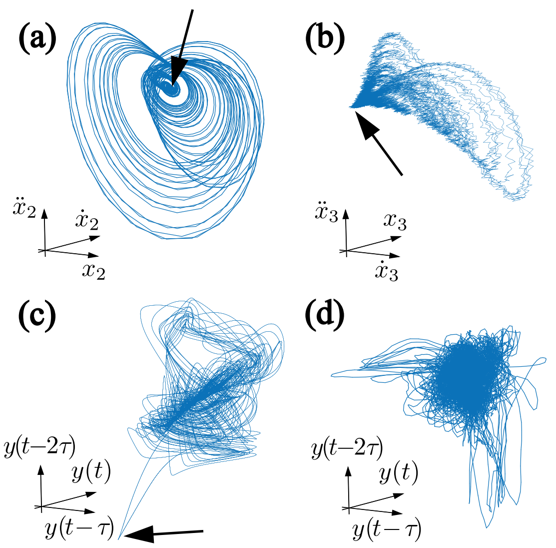

FIG. 11. Embedded attractors of different dynamical systems. Differential embedding coordinates of the (a) Cord system and (b) Rössler system. Time-delay embedding coordinates of the (c) Epileptor model and (d) human EEG data. Unobservable regions in subplots (a)–(c) are pointed out by arrows.

time-series data, which, as we show next, has a high correlation with the coefficients of observability [Fig. 12(d)].

Figures 12(a)–12(c) shows the coefficient of functional observability and the tSVD for a given time series $y(t)$. For the deterministic model, κ and σ_{d_e} are anticorrelated: as κ increases (decreases) during normal (seizure) regimes of the Epileptor, the tSVD decreases (increases). The anticorrelation is confirmed by a Pearson's correlation index of $\rho = -0.96$ between both coefficients in logarithmic scale [Fig. 12(d), top]. As expected, when the Epileptor switches to the normal region, which is poorly functionally observable ($\kappa > 10^4$), the smallest singular value σ_{d_e} tends to zero ($\sigma_{d_e} \approx 10^{-16}$), implying an effective loss of dimension of the embedded time series. For the stochastic model, the broader state-space exploration of this system yields a higher variation of κ and σ_{d_e}. Nevertheless, the same anticorrelation between κ and σ_{d_e} can be observed by smoothing the coefficients over a moving average window. On average, κ (σ_{d_e}) increases (decreases) during the normal regime of the Epileptor, yielding a Pearson's correlation index of $\rho = -0.82$ [Fig. 12(d), bottom].

The behavior of the tSVD measure is remarkably aligned with that of typical early-warning signals used to detect critical transitions from time-series data [74], including those for seizure warning from EEG data [75]. Indeed, there is a sharp increase of the tSVD close to the dynamical transition from normal to seizure state [Fig. 12(c)]. This may be attributed to the Epileptor's unobservability at the saddle-node bifurcation point, as pinpointed in Sec. V A. Figure 11(c) shows that the embedded trajectories squeeze to singularity point at the unobservable (bifurcation) point—a feature that can be further explored for early-warning detection of seizure events. This topological characteristic of the embedded attractor is present not only in the Epileptor model but also in real data, as shown in Fig. 11(d) for the embedding space constructed from human intracranial EEG data (public data available at [73]; sampling protocols and preliminary analysis are described in [68]). Further computing the tSVD in human EEG data provides interesting results as illustrated for a representative patient in Fig. 13: The seizure onset is often preceded by a decrease of σ_{d_e} followed by a sharp increase close to the critical transition, a characteristic that may be explored for real-time monitoring and detection of seizure events. The same pattern was observed for all patients in the considered dataset, although a thorough statistical investigation of the tSVD as a early-warning signal of seizure events (and other critical transitions in complex systems) is left for future work.

VI. DISCUSSION

The established relation between observability and embedding theories opens a new research direction of special interest to (nonlinear) time-series analysis. Our theory formally determines the conditions for reconstructing the system state from time-series data, often low-dimensional or univariate. In fact, measuring every relevant state variable is in practice constrained by physical limitations or operational costs. Hence, indirect estimation of unmeasured variables is required for the observation of physical, biological, ecological, and other complex dynamical systems.

For applications, which require reconstructing only a few key state variables or lower-dimensional subspaces, we formalize the notion of functional observability for nonlinear systems. Our results can provide *a priori* knowledge of the reconstruction limitations and embedding features, depending on the available time-series data. We show that, even if a system is not completely observable (reconstructible), it may still be functionally observable with respect to the variables or subspace of interest. This provides useful insights about the dynamical system's properties and can be used to guide experimental design and data-processing methods according to the investigated hypotheses and available measurement processes.

In the context of systems biology, observing system dynamics is often hampered by technical limitations that prevent the simultaneous measurement of multiple biophysical variables (e.g., multiple ion channels in single neurons). By identifying conditions for accurate inference of variables from time-series data, the presented functional observability analysis can thus guide experimental design. Consider, for example, the HR neuron model investigated in Sec. IV C. The fast recovery current and the slow adaptation current represented by the system's state variables are related to transport rates of fast (e.g., sodium and potassium) and slow (e.g., calcium) ion channels, respectively [66]. Our analysis reveals structural limitations in the HR neuron model that prevent an accurate inference of calcium flux from measures of sodium/potassium fluxes. The opposite, instead, seems feasible, given that the system is completely observable everywhere when inferring sodium/potassium flux from measures of calcium flux.

Likewise, in a biomedical context, evaluating the functional observability of the Epileptor model shows that reconstructing the slow permittivity variable from EEG data ($y = x_1 + x_4$) is complicated by the system's poor observability in the attractor's normal state (Sec. V). Contrariwise, independently measuring the state variables x_1 and x_4 (i.e.,

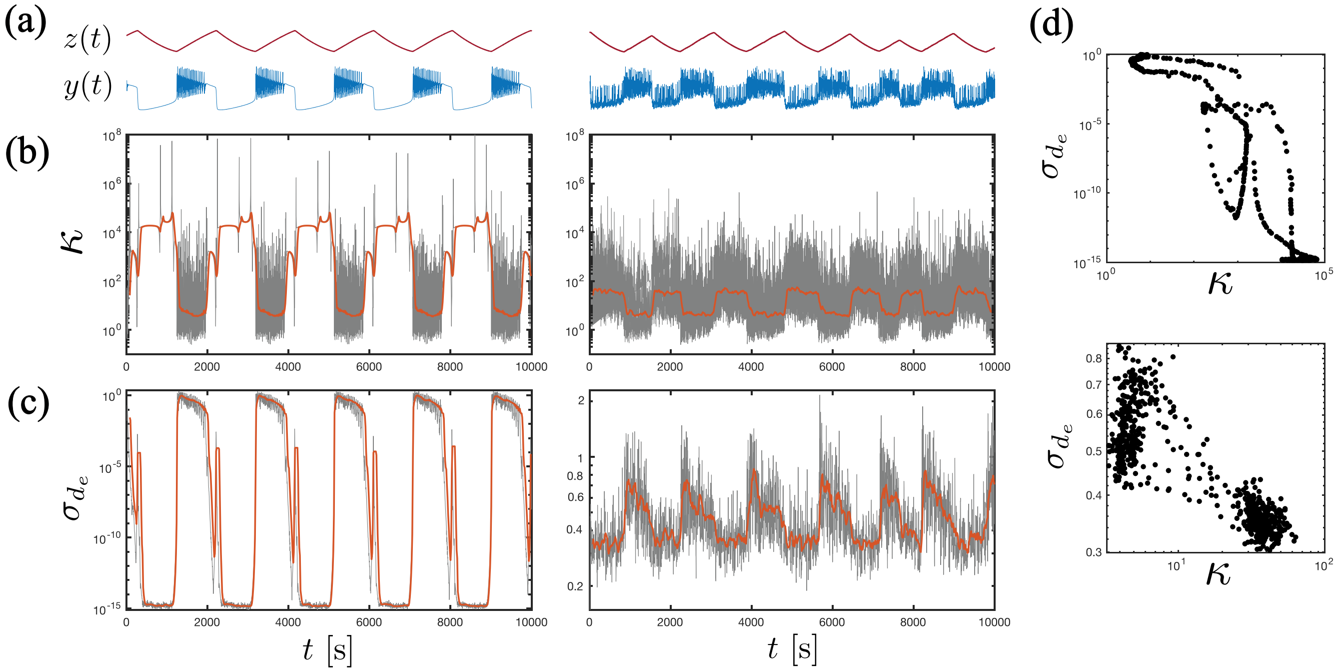

FIG. 12. Observability and early-warning signal of the deterministic (left) and stochastic (right) Epileptor models. (a) Time series of the functional $z(t)$ and the measured signal $y(t)$. In the stochastic case, noise can trigger more transitions for the same time interval. (b) Coefficient of functional observability κ as a function of time. (c) tSVD σ_{d_e} as a function of time, computed over a moving time-series window with length $N = 5$s and embedding parameters $(d_e, \tau) = (5, 0.1\text{s})$. Orange curves show the smoothed coefficients computed over a moving average window with length $N_{\text{avg}} = 150$ s, sampled every 30 s. (d) Correlation between κ and σ_{d_e} for the deterministic (top) and stochastic (bottom) system.

$y = [x_1 \;\; x_4]^\mathsf{T}$) yields well-conditioned coefficients of observability throughout the entire attractor. This suggests that applying data preprocessing methods in EEG time series to decouple the oscillatory behavior (modeled by x_1) from the spikes and wave components (modeled by x_4) may lead to better performance in reconstructing the permittivity variable for early-warning of seizures.

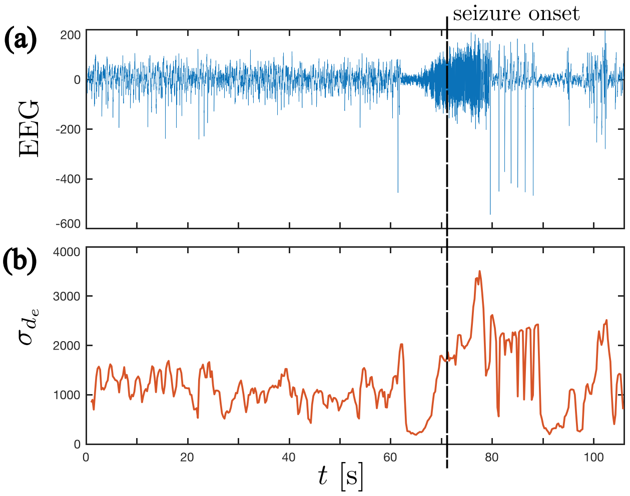

FIG. 13. Early warning of seizure events in human intracranial EEG data. (a) Intracranial EEG data (channel 2) of patient 10 in database [73]. (b) tSVD σ_{d_e} computed over a moving time-series window with parameters $(d_e, \tau, N) = (5, 0.05\text{ s}, 1\text{ s})$. Seizure onset (informed by expert opinion) is marked by the dashed line.

In addition to applications, the proposed theory opens new theoretical research directions for many disciplines. First, the Cord and HR neuron examples show interesting links between the functional observability of a system and its intrinsic timescales. In both cases, high reconstruction errors stem from estimating slow variables from measures of fast variables. Future works can formally explore this interesting relation, complementing the analysis for linear systems [76], by extending the notion of functional observability to (nonlinear) differential-algebraic systems of form

$$\begin{aligned} \dot{\boldsymbol{x}}_1 &= \boldsymbol{f}_1(\boldsymbol{x}_1, \boldsymbol{x}_2), \\ 0 &= \boldsymbol{f}_2(\boldsymbol{x}_1, \boldsymbol{x}_2), \end{aligned} \tag{42}$$

where a strong timescale separation arises from a quasi-steady-state assumption ($\dot{\boldsymbol{x}}_2 \approx 0$).

Second, our analysis of the Epileptor model shows a potential relation between the system's observability and its bifurcation points. Whether the loss of observability close to critical transitions is a universal behavior or a particularity of the Epileptor remains to be investigated. In ecological networks, time-series data of variables that make the system completely observable often lead to earlier warning of critical transitions [32]. Our time-series-based coefficient tSVD, aside from indirectly quantifying observability, may also capture features related to the central limit theorem [77] (that, close to bifurcation points, dynamical systems can be locally reduced to low-dimensional normal forms). However, it is still to be investigated whether our framework only applies to transitions induced by local bifurcations, or it can be extended to other types like boundary crisis involving chaotic attractors [78,79].

The potential use of tSVD for early-warning detection of critical transitions in complex systems, similar to other signals like increasing variance and autocorrelation [74,80], may lead to promising theoretical developments and applications.

Third, our theory fosters data-driven methods for the automated construction of the embedding space, and its map $\mathbf{\Phi}$ to the original system's attractor, in applications where analytical analysis of the model is untractable (e.g., due to unknown parameters or high dimensionality). This would thus extend previous works on automated embedding construction [81] and full system identification from embedding coordinates [82]. Although our application examples focus on univariate measurements and functionals, the theory is formalized for multivariate cases ($q, r \geqslant 1$) and can be directly applied to determine the existence and conditioning of such map, assessing how good the reconstruction is expected to be (locally).

Finally, for the study of high-dimensional problems, our results call for extensions based on graph-theoretical conditions [31,37,52] or network motifs [35]. In fact, as the computation of Lie derivatives is particularly demanding for high-dimensional systems, scalable strategies have yet to be developed to investigate the functional observability of large-scale nonlinear networks.

ACKNOWLEDGMENTS

The authors thank Dr. Cristina Donato for useful insights on seizure onset. L.F. acknowledges support from Brazil's Fundação de Amparo à Pesquisa do Estado de Minas Gerais (Grant No. APQ-00781-21) and Conselho Nacional de Desenvolvimento Científico e Tecnológico (Grant No. 409487/2021-0). D.P. is supported by the Luxembourg National Research Fund (Grant No. PRIDE DTU CriTiCS 10907093).

APPENDIX A: PROOF OF THEOREM 2

Proof. Given sufficiently smooth functions $f(\boldsymbol{x})$ and $\boldsymbol{h}(\boldsymbol{x})$, we show that condition (16) holds if and only if condition (18) holds.

Sufficiency. If condition (16) holds, then there exists some matrices $L_i \in \mathbb{R}^{r\times q}$, $i = 1, \dots, s$, such that

$$\nabla\mathcal{L}_f^0\boldsymbol{g}(\boldsymbol{x}) = \sum_{i=0}^{s} L_i \nabla\mathcal{L}_f^i\boldsymbol{h}(\boldsymbol{x}). \tag{A1}$$

Thus, condition (18) holds given that $\mathcal{L}_f^0\boldsymbol{g}(\boldsymbol{x}) = \boldsymbol{g}(\boldsymbol{x})$.

Necessity. If condition (18) is satisfied, then relation (A1) holds. Right-multiplying (A1) by $\boldsymbol{f}(\boldsymbol{x})$ yields

$$\mathcal{L}_f^1\boldsymbol{g}(\boldsymbol{x}) = \sum_{i=0}^{s} L_i \mathcal{L}_f^{i+1}\boldsymbol{h}(\boldsymbol{x}). \tag{A2}$$

By induction, successively taking the gradient on both sides yields

$$\begin{aligned}\nabla\mathcal{L}_f^1\boldsymbol{g}(\boldsymbol{x}) &= \sum_{i=1}^{s+1} L_{i1} \nabla\mathcal{L}_f^i\boldsymbol{h}(\boldsymbol{x}),\\ &\vdots\\ \nabla\mathcal{L}_f^\mu\boldsymbol{g}(\boldsymbol{x}) &= \sum_{i=\mu}^{s+\mu} L_{i\mu} \nabla\mathcal{L}_f^i\boldsymbol{h}(\boldsymbol{x}),\end{aligned} \tag{A3}$$

for some matrices $L_{ij} \in \mathbb{R}^{r\times q}$, $i = 1, \dots, s$ and $j = 1, \dots, \mu$. From Definition 2, $\nabla\mathcal{L}_f^{s+j}\boldsymbol{h}(\boldsymbol{x})$ is a linear combination of $\{\nabla\mathcal{L}_f^0\boldsymbol{h}(\boldsymbol{x}), \dots, \nabla\mathcal{L}_f^s\boldsymbol{h}(\boldsymbol{x})\}$. Therefore, equations (A3) can be expressed as

$$\nabla\mathcal{L}_f^j\boldsymbol{g}(\boldsymbol{x}) = \sum_{i=0}^{s} L_{ij} \nabla\mathcal{L}_f^i\boldsymbol{h}(\boldsymbol{x}), \tag{A4}$$

which implies that condition (16) is satisfied. ■

APPENDIX B: COEFFICIENTS OF OBSERVABILITY FROM TIME-SERIES DATA

The coefficients of observability (30) can be indirectly inferred from time-series data by exploring the topological features associated with unobservable regions in the embedded state space. Let $Y(t) \in \mathbb{R}^N$ be the recorded time-series data, for time instants $t \in [0, N]$, and $X = [Y(t)\ Y(t-\tau)\ \dots\ Y(t-(d_e-1)\tau)] \in \mathbb{R}^{N\times d_e}$ be the corresponding time-delay embedding for some embedding dimension d_e and delay τ. Methods based on singular value decomposition of embedded time-series data were shown to indirectly quantify the system's local observability, by measuring the geometrical complexity around some neighborhood of the embedded attractor to identify singularities in the embedded trajectories [23,83].

Here, we indirectly measure the system's observability by monitoring the smallest singular value σ_{d_e} corresponding to the singular value decomposition $X = U\Sigma V^\intercal$. Note that the subindex d_e corresponds to the embedding dimension. The coefficient σ_{d_e} is addressed as tSVD throughout the paper. To compare the local coefficient of functional observability $\kappa(t)$ at some time instant t to the tSVD $\sigma_{d_e}(t)$ (Fig. 12), $\sigma_{d_e}(t)$ must be locally computed using a short time-series window close to the time instant t. In this paper, we consider that $\sigma_{d_e}(t)$ is computed using the embedding of a moving time-series window of length N: $\{X(t-N), \dots, X(t)\}$. Since numerical results may show high variability, we can also use a second moving average window of length N_{avg} to smooth the computed tSVD.

---

[1] T. Sauer, J. A. Yorke, and M. Casdagli, Embedology, J. Stat. Phys. **65**, 579 (1991).

[2] N. Marwan, J. F. Donges, Y. Zou, R. V. Donner, and J. Kurths, Complex network approach for recurrence analysis of time series, Phys. Lett. A **373**, 4246 (2009).

[3] J. Lekscha and R. V. Donner, Phase space reconstruction for non-uniformly sampled noisy time series, Chaos **28**, 085702 (2018).

[4] U. Bhat and S. B. Munch, Recurrent neural networks for partially observed dynamical systems, Phys. Rev. E **105**, 044205 (2022).

[5] M. B. Kennel and S. Isabelle, Method to distinguish possible chaos from colored noise and to determine embedding parameters, Phys. Rev. A **46**, 3111 (1992).

[6] N. Marwan, M. Carmen Romano, M. Thiel, and J. Kurths, Recurrence plots for the analysis of complex systems, Phys. Rep. **438**, 237 (2007).

[7] G. Sugihara, R. May, H. Ye, C. H. Hsieh, E. Deyle, M. Fogarty, and S. Munch, Detecting causality in complex ecosystems, Science **338**, 496 (2012).

[8] A. Groth and M. Ghil, Synchronization of world economic activity, Chaos **27**, 127002 (2017).

[9] R. d. A. Araújo, N. Nedjah, A. L. Oliveira, and S. R. L. Meira, A deep increasing–decreasing-linear neural network for financial time series prediction, Neurocomputing **347**, 59 (2019).

[10] M. Gidea, D. Goldsmith, Y. Katz, P. Roldan, and Y. Shmalo, Topological recognition of critical transitions in time series of cryptocurrencies, Physica A **548**, 123843 (2020).

[11] N. C. Carvalho, L. L. Portes, A. Beda, L. M. Tallarico, and L. A. Aguirre, Recurrence plots for the assessment of patient-ventilator interactions quality during invasive mechanical ventilation, Chaos **28**, 085707 (2018).

[12] P. A. Pérez-Toro, J. C. Vásquez-Correa, T. Arias-Vergara, E. Nöth, and J. R. Orozco-Arroyave, Nonlinear dynamics and Poincaré sections to model gait impairments in different stages of Parkinson's disease, Nonlinear Dyn. **100**, 3253 (2020).

[13] J. Lekscha and R. V. Donner, Detecting dynamical anomalies in time series from different palaeoclimate proxy archives using windowed recurrence network analysis, Nonlinear Process. Geophys. **27**, 261 (2020).

[14] Z. K. Gao, X. W. Zhang, N. D. Jin, R. V. Donner, N. Marwan, and J. Kurths, Recurrence networks from multivariate signals for uncovering dynamic transitions of horizontal oil-water stratified flows, Europhys. Lett. **103**, 50004 (2013).

[15] C. Letellier, L. A. Aguirre, and J. Maquet, Relation between observability and differential embeddings for nonlinear dynamics, Phys. Rev. E **71**, 066213 (2005).

[16] L. A. Aguirre and C. Letellier, Observability of multivariate differential embeddings, J. Phys. A: Math. Gen. **38**, 6311 (2005).

[17] R. Kalman, On the general theory of control systems, IEEE Trans. Automat. Contr. **4**, 110 (1959).

[18] G. Luenberger, Observers for multivariable systems, IEEE Trans. Automat. Contr. **11**, 190 (1966).

[19] R. E. Kalman, A new approach to linear filtering and prediction problems, Trans. ASME–J. Basic Eng. **82**, 35 (1960).

[20] R. Hermann and A. J. Krener, Nonlinear Controllability and Observability, IEEE Trans. Automat. Contr. **22**, 728 (1977).

[21] L. M. Pecora and T. L. Carroll, Synchronization in Chaotic Systems, Phys. Rev. Lett. **64**, 821 (1990).

[22] C. Letellier and L. A. Aguirre, Investigating nonlinear dynamics from time series: The influence of symmetries and the choice of observables, Chaos **12**, 549 (2002).

[23] L. L. Portes and L. A. Aguirre, Enhancing multivariate singular spectrum analysis for phase synchronization: The role of observability, Chaos **26**, 093112 (2016).

[24] T. L. Carroll, Testing dynamical system variables for reconstruction, Chaos **28**, 103117 (2018).

[25] L. L. Portes, A. N. Montanari, D. C. Correa, M. Small, and L. A. Aguirre, The reliability of recurrence network analysis is influenced by the observability properties of the recorded time series, Chaos **29**, 083101 (2019).

[26] A. Haber, F. Molnar, and A. E. Motter, State observation and sensor selection for nonlinear networks, IEEE Trans. Control Netw. Syst. **5**, 694 (2018).

[27] J. Guan, T. Berry, and T. Sauer, Limits on reconstruction of dynamical networks, Phys. Rev. E **98**, 022318 (2018).

[28] A. N. Montanari and L. A. Aguirre, Particle filtering of dynamical networks: Highlighting observability issues, Chaos **29**, 033118 (2019).

[29] F. Su, J. Wang, H. Li, B. Deng, H. Yu, and C. Liu, Analysis and application of neuronal network controllability and observability, Chaos **27**, 023103 (2017).

[30] L. A. Aguirre, L. L. Portes, and C. Letellier, Observability and synchronization of neuron models, Chaos **27**, 103103 (2017).

[31] Y.-Y. Liu, J.-J. Slotine, and A.-L. Barabási, Observability of complex systems, Proc. Natl. Acad. Sci. USA **110**, 2460 (2013).

[32] A. Aparicio, J. X. Velasco-Hernández, C. H. Moog, Y. Y. Liu, and M. T. Angulo, Structure-based identification of sensor species for anticipating critical transitions, Proc. Natl. Acad. Sci. USA **118**, e2104732118 (2021).

[33] F. Pasqualetti, S. Zampieri, and F. Bullo, Controllability, limitations and algorithms for complex networks, IEEE Trans. Control Netw. Syst. **1**, 40 (2013).

[34] J. Sun and A. E. Motter, Controllability Transition and Nonlocality in Network Control, Phys. Rev. Lett. **110**, 208701 (2013).

[35] A. J. Whalen, S. N. Brennan, T. D. Sauer, and S. J. Schiff, Observability and Controllability of Nonlinear Networks: The Role of Symmetry, Phys. Rev. X **5**, 011005 (2015).

[36] C. Letellier, I. Sendiña-Nadal, and L. A. Aguirre, A nonlinear graph-based theory for dynamical network observability, Phys. Rev. E **98**, 020303(R) (2018).

[37] M. T. Angulo, A. Aparicio, and C. H. Moog, Structural accessibility and structural observability of nonlinear networked systems, IEEE Trans. Netw. Sci. Eng. **7**, 1656 (2020).

[38] A. N. Montanari and L. A. Aguirre, Observability of network systems: A critical review of recent results, J. Control Autom. Electr. Syst. **31**, 1348 (2020).

[39] M. G. Rosenblum, A. S. Pikovsky, and J. Kurths, From Phase to Lag Synchronization in Coupled Chaotic Oscillators, Phys. Rev. Lett. **78**, 4193 (1997).

[40] L. Freitas, L. A. B. Torres, and L. A. Aguirre, Phase definition to assess synchronization quality of nonlinear oscillators, Phys. Rev. E **97**, 052202 (2018).

[41] J. Oh, E. Reischmann, and J. A. Rial, Polar synchronization and the synchronized climatic history of Greenland and Antarctica, Quat. Sci. Rev. **83**, 129 (2014).

[42] D. Smug, P. Ashwin, and D. Sornette, Predicting financial market crashes using ghost singularities, PLoS One **13**, e0195265 (2018).

[43] W. Youn, M. B. Rhudy, A. Cho, and H. Myung, Fuzzy adaptive attitude estimation for a fixed-wing UAV with a virtual SSA sensor during a GPS outage, IEEE Sens. J. **20**, 1456 (2020).

[44] T. Quail, A. Shrier, and L. Glass, Predicting the onset of period-doubling bifurcations in noisy cardiac systems, Proc. Natl. Acad. Sci. USA **112**, 9358 (2015).

[45] V. K. Jirsa, W. C. Stacey, P. P. Quilichini, A. I. Ivanov, and C. Bernard, On the nature of seizure dynamics, Brain **137**, 2210 (2014).

[46] T. L. Fernando, H. M. Trinh, and L. Jennings, Functional observability and the design of minimum order linear

functional observers, IEEE Trans. Auto. Control **55**, 1268 (2010).

[47] L. S. Jennings, T. L. Fernando, and H. M. Trinh, Existence conditions for functional observability from an eigenspace perspective, IEEE Tran. Auto. Control **56**, 2957 (2011).

[48] M. Darouach, Existence and design of functional observers for linear systems, IEEE Trans. Auto. Control **45**, 940 (2000).

[49] T. Hieu and F. Tyrone, *Functional Observers for Dynamical Systems* (Springer, Berlin, 2012).

[50] H. H. Alhelou, M. E. H. Golshan, and N. D. Hatziargyriou, A decentralized functional observer based optimal LFC considering unknown inputs, uncertainties, and cyber-attacks, IEEE Trans. Power Syst. **34**, 4408 (2019).

[51] K. Emami, T. Fernando, B. Nener, H. Trinh, and Y. Zhang, A functional observer based fault detection technique for dynamical systems, J. Franklin Inst. **352**, 2113 (2015).

[52] A. N. Montanari, C. Duan, L. A. Aguirre, and A. E. Motter, Functional observability and target state estimation in large-scale networks, Proc. Natl. Acad. Sci. USA **119**, e2113750119 (2021).

[53] M. Vidyasagar, *Nonlinear Systems Analysis*, 2nd ed. (Prentice Hall, Englewood Cliffs, NJ, 1978).

[54] M. Anguelova, Nonlinear Observability and Identifiability: General Theory and a Case Study of a Kinetic Model for S. cerevisiae, Ph.D. thesis, Chalmers University of Technology and Göteborg University, 2004.

[55] C.-T. Chen, *Linear System Theory and Design*, 3rd ed. (Oxford University Press, Oxford, 1999).

[56] L. I. Rudin, S. Osher, and E. Fatemi, Nonlinear total variation based noise removal algorithms, Physica D **60**, 259 (1992).

[57] R. Chartrand, Numerical differentiation of noisy, nonsmooth data, Intl. Sch. Res. Notices **2011**, 164564 (2011).

[58] F. Takens, Detecting strange attractors in turbulence, in *Dynamical Systems and Turbulence*, edited by D. Rand and L. Young (Springer, Berlin, 1981) pp. 366–381.

[59] J. Stark, D. S. Broomhead, M. E. Davies, and J. Huke, Takens embedding theorems for forced and stochastic systems, Nonlinear Anal.: Theory Methods Appl. **30**, 5303 (1997).

[60] F. Rotella and I. Zambettakis, A note on functional observability, IEEE Trans. Auto. Control **61**, 3197 (2016).

[61] https://github.com/montanariarthur/NonlinearObservability.

[62] C. Letellier and L. A. Aguirre, Required criteria for recognizing new types of chaos: Application to the "cord" attractor, Phys. Rev. E **85**, 036204 (2012).

[63] L. Freitas, L. L. Portes, L. A. B. Torres, and L. A. Aguirre, Phase coherence is not related to topology, Phys. Rev. E **101**, 032207 (2020).

[64] J. L. Hindmarsh and R. M. Rose, A model of neuronal bursting using three coupled first order differential equations, Proc. R. Soc. London B **221**, 87 (1984).

[65] M. Storace, D. Linaro, and E. De Lange, The Hindmarsh-Rose neuron model: Bifurcation analysis and piecewise-linear approximations, Chaos **18**, 033128 (2008).

[66] H. Gu, Biological experimental observations of an unnoticed chaos as simulated by the Hindmarsh-Rose model, PLoS One **8**, e81759 (2013).

[67] F. Mormann, R. G. Andrzejak, C. E. Elger, and K. Lehnertz, Seizure prediction: The long and winding road, Brain **130**, 314 (2007).

[68] M. J. Cook, T. J. O'Brien, S. F. Berkovic, M. Murphy, A. Morokoff, G. Fabinyi, W. D'Souza, R. Yerra, J. Archer, L. Litewka *et al.*, Prediction of seizure likelihood with a long-term, implanted seizure advisory system in patients with drug-resistant epilepsy: A first-in-man study, Lancet Neuro. **12**, 563 (2013).

[69] L. Kuhlmann, P. Karoly, D. R. Freestone, B. H. Brinkmann, A. Temko, A. Barachant, F. Li, G. Titericz Jr, B. W. Lang, D. Lavery *et al.*, Epilepsyecosystem.org: Crowd-sourcing reproducible seizure prediction with long-term human intracranial EEG, Brain **141**, 2619 (2018).

[70] Y. Yuan, Y. Li, and D. P. Mandic, Comparison analysis of embedding dimension between normal and epileptic EEG time series, J. Physiol. Sci. **58**, 239 (2008).

[71] K. El Houssaini, C. Bernard, and V. K. Jirsa, The epileptor model: A systematic mathematical analysis linked to the dynamics of seizures, refractory status epilepticus, and depolarization block, eNeuro **7**, ENEURO.0485-18.2019 (2020).

[72] M. Scheffer, J. Bascompte, W. A. Brock, V. Brovkin, S. R. Carpenter, V. Dakos, H. Held, E. H. Van Nes, M. Rietkerk, and G. Sugihara, Early-warning signals for critical transitions, Nature (London) **461**, 53 (2009).

[73] P. Karoly, M. Cook, L. Kuhlmann, D. Freestone, D. Grayden, E. Nurse, A. Lai, D. Payne, W. D'Souza, U. Seneviratne *et al.*, Melbourne NeuroVista Seizure Prediction Trial, University of Melbourne. Dataset (2018), doi: 10.26188/5b6a999fa2316.

[74] C. Kuehn, A mathematical framework for critical transitions: Bifurcations, fast–slow systems and stochastic dynamics, Physica D **240**, 1020 (2011).

[75] M. I. Maturana, C. Meisel, K. Dell, P. J. Karoly, W. D'Souza, D. B. Grayden, A. N. Burkitt, P. Jiruska, J. Kudlacek, J. Hlinka *et al.*, Critical slowing down as a biomarker for seizure susceptibility, Nat. Commun. **11**, 2172 (2020).

[76] T. Berger, T. Reis, and S. Trenn, Observability of linear differential-algebraic systems: A survey, in *Surveys in Differential-Algebraic Equations IV* (Springer International Publishing, New York, 2017) pp. 161–219.

[77] M. Haragus and G. Iooss, *Local Bifurcation, Center Manifolds and Normal Forms in Infinte-Dimensional Dynamical Systems* (Springer Science & Business Media, New York, 2010).

[78] A. Tantet, V. Lucarini, and H. A. Dijkstra, Resonances in a chaotic attractor crisis of the Lorenz flow, J. Stat. Phys. **170**, 584 (2018).

[79] A. Tantet, V. Lucarini, F. Lunkeit, and H. A. Dijkstra, Crisis of the chaotic attractor of a climate model: A transfer operator approach, Nonlinearity **31**, 2221 (2018).

[80] D. Proverbio, A. N. Montanari, A. Skupin, and J. Gonçalves, Buffering variability in cell regulation motifs close to criticality, Phys. Rev. E **106**, L032402 (2022).

[81] A. Sadeghzadeh and R. Tóth, Improved embedding of nonlinear systems in linear parameter-varying models with polynomial dependence, IEEE Trans. Control Syst. Technol. (2022).

[82] S. L. Brunton, J. L. Proctor, and J. N. Kutz, Discovering governing equations from data by sparse identification of nonlinear dynamical systems, Proc. Natl. Acad. Sci. USA **113**, 3932 (2016).

[83] L. A. Aguirre and C. Letellier, Investigating observability properties from data in nonlinear dynamics, Phys. Rev. E **83**, 066209 (2011).